Diagnosing CO2 emission-induced feedbacks between the Southern Ocean carbon cycle and the climate system: A multiple Earth System Model analysis using a water mass tracking approach

Tilla Roy, Jean-Baptiste Sallée, Laurent Bopp, Nicolas Metzl

To cite this version:

Tilla Roy, Jean-Baptiste Sallée, Laurent Bopp, Nicolas Metzl. Diagnosing CO2 emission-induced feedbacks between the Southern Ocean carbon cycle and the climate system: A multiple Earth System Model analysis using a water mass tracking approach. Journal of Climate, 2021, 34 (22), pp.9071-9082. 10.1175/JCLI-D-20-0889.1 . hal-03607283

HAL Id: hal-03607283
https://hal.science/hal-03607283

Submitted on 13 Mar 2022

Diagnosing CO_2-Emission-Induced Feedbacks between the Southern Ocean Carbon Cycle and the Climate System: A Multiple Earth System Model Analysis Using a Water Mass Tracking Approach

TILLA ROY,[a,b] JEAN BAPTISTE SALLÉE,[c] LAURENT BOPP,[a] AND NICOLAS METZL[c]

[a] *LMD-IPSL, Ecole Normale Supérieure/Université PSL, CNRS, Sorbonne Université, Ecole Polytechnique, Paris, France*
[b] *ECOCEANA, Paris, France*
[c] *Sorbonne Université, LOCEAN-IPSL, CNRS, IRD, MHNH, Paris, France*

(Manuscript received 20 November 2020, in final form 10 May 2021)

ABSTRACT: Anthropogenic CO_2-emission-induced feedbacks between the carbon cycle and the climate system perturb the efficiency of atmospheric CO_2 uptake by land and ocean carbon reservoirs. The Southern Ocean is a region where these feedbacks can be largest and differ most among Earth system model projections of twenty-first-century climate change. To improve our mechanistic understanding of these feedbacks, we develop an automated procedure that tracks changes in the positions of Southern Ocean water masses and their carbon uptake. In an idealized ensemble of climate change projections, we diagnose two carbon–concentration feedbacks driven by atmospheric CO_2 (due to increasing air–sea CO_2 partial pressure difference, $dpCO_2$, and reducing carbonate buffering capacity) and two carbon–climate feedbacks driven by climate change (due to changes in the water mass surface outcrop areas and local climate impacts). Collectively these feedbacks increase the CO_2 uptake by the Southern Ocean and account for almost one-fourth of the global uptake of CO_2 emissions. The increase in CO_2 uptake is primarily $dpCO_2$ driven, with Antarctic Intermediate Waters making the largest contribution; the remaining three feedbacks partially offset this increase (by ~25%), with maximum reductions in Subantarctic Mode Waters. The process dominating the decrease in CO_2 uptake is water mass dependent: reduction in carbonate buffering capacity in Subtropical and Subantarctic Mode Waters, local climate impacts in Antarctic Intermediate Waters, and reduction in outcrop areas in Circumpolar Deep Waters and Antarctic Bottom Waters. Intermodel variability in the feedbacks is predominately $dpCO_2$ driven and should be a focus of efforts to constrain projection uncertainty.

KEYWORDS: Southern Ocean; Carbon cycle; Model comparison

1. Introduction

Anthropogenic CO_2 emissions (C_E) induce feedbacks between the global carbon cycle and the climate system (hereafter carbon cycle feedbacks) by perturbing the efficiency of atmospheric CO_2 uptake and storage by the ocean (ΔC_O; Sarmiento et al. 1998) and land (ΔC_L; Cao and Woodward 1998) reservoirs and causing the atmospheric carbon reservoir (ΔC_A) to rise faster or slower than expected from anthropogenic CO_2 emissions alone (Sarmiento et al. 1995; Cox et al. 2000; Friedlingstein et al. 2003):

$$C_E = \Delta C_A + \Delta C_L + \Delta C_O. \quad (1)$$

Uncertainty in the magnitudes of carbon cycle feedbacks hamper our confidence in projections of future climate and estimates of allowable anthropogenic carbon emissions for given climate targets (Jones et al. 2013).

To diagnose carbon cycle feedbacks in Earth system models (ESMs) several approaches have been developed (Friedlingstein et al. 2006; Gregory et al. 2009; Arora et al. 2013, 2020). Common to these approaches is the partitioning of the change in carbon uptake by the land/ocean carbon reservoirs into two feedbacks: the *carbon–concentration feedback* that is driven by changes to atmospheric CO_2 concentrations (no climate change) and the *carbon–climate feedback* that is driven by changes in radiative forcing and subsequent climate change. The strength of these feedbacks is characterized by two feedback sensitivity parameters: β for the carbon–concentration feedback and γ for the carbon–climate feedback. These feedbacks parameters can be characterized globally, regionally, or spatially, and temporally. A *positive* β or γ represents an increase in carbon uptake/storage by the ocean/land reservoir and, consequently, a *negative* carbon cycle feedback from the perspective of the atmosphere or the climate system (i.e., dampening of global warming because less CO_2 is retained in the atmosphere), and vice versa for a negative β or γ. Also, an increase in β or γ over time implies that the feedback is increasing the atmospheric CO_2 uptake efficiency of the ocean/land reservoir, and vice versa for a decrease in β or γ.

The strength of the ocean carbon–concentration feedback (β) is predominately a balance between two opposing atmospheric CO_2-driven chemical perturbations to the marine carbon cycle. First the transient increase in atmospheric CO_2 uptake by the ocean due to the increasing partial pressure difference between the surface ocean and atmosphere, $dpCO_2$,

---

Denotes content that is immediately available upon publication as open access.

Supplemental information related to this paper is available at the Journals Online website: https://doi.org/10.1175/JCLI-D-20-0889.s1.

Corresponding author: Tilla Roy, tilla.roy@ecoceana.org

DOI: 10.1175/JCLI-D-20-0889.1

where $dpCO_2 = pCO_2o - pCO_2a$ (positive contribution to β). Second, the chemically driven decrease in atmospheric CO_2 uptake by the ocean due to the reduction in carbonate buffering capacity (negative contribution to β), which has long been recognized as one of the largest positive marine carbon cycle feedbacks on atmospheric CO_2 (Siegenthaler and Oeschger 1978; Sarmiento et al. 1995; Wallace 2001; Jiang et al. 2019). It is also well characterized because its mechanism is rooted in fundamental inorganic carbon chemistry (Revelle and Suess 1957; Zeebe and Wolf-Gladrow 2001; Sarmiento 2013).

Many of the simulated processes contributing to the strength of the carbon–climate feedback (γ) were characterized (Maier-Reimer et al. 1996; Sarmiento and Le Quéré 1996; Joos et al. 1999; Sarmiento et al. 1998; Matear and Hirst 1999; Plattner et al. 2001) well before their net contribution to γ was quantified in ESMs (Friedlingstein et al. 2003, 2006; Roy et al. 2011; Schwinger et al. 2014), including changes to (i) ocean temperature, whereby warming consistently reduces the solubility of CO_2 driving a net global outgassing of oceanic carbon (negative contribution to γ); (ii) ocean circulation, whereby the supply of dissolved inorganic carbon (DIC) to the ocean surface is perturbed via changes to physical processes including stratification, obduction/subduction, and vertical and horizontal entrainment (positive/negative contribution to γ); and (iii) biological productivity, whereby the transport of carbon associated with biological matter is perturbed (positive/negative contribution to γ). Because of the complex interplay of these processes that modify ocean carbon uptake over different spatial and temporal scales, it remains difficult to disentangle their relative contribution in ensembles of climate projections. Furthermore, the geographical region and the mechanisms dominating the magnitude of global γ, differ between the model projections (Roy et al. 2011).

The Southern Ocean (SO) is one of the regions where the projected carbon cycle feedbacks can be largest and where they differ most between the models (Friedlingstein et al. 2003; Roy et al. 2011; Hewitt et al. 2016). In the Southern Ocean, both the *natural* (preindustrial) and the *anthropogenic* (associated with anthropogenic CO_2 emissions) air–sea CO_2 fluxes are major contributors to the global air–sea exchange of CO_2. Consequently, even relatively small changes to Southern Ocean processes can produce large perturbations to the balance of carbon between the ocean and atmosphere (Sigman et al. 2010; Landschützer et al. 2015).

Both the *natural* (preindustrial) and the *anthropogenic* (associated with anthropogenic CO_2 emissions) air–sea CO_2 fluxes are intimately linked to the southern limb of the meridional overturning circulation (MOC; Marshall and Speer 2012) [see comprehensive reviews in Takahashi et al. (2012) and Gruber et al. (2019)]. The natural component is dominated by outgassing where Circumpolar Deep Waters (CDW) rich in DIC are ventilated—around and south of the polar front—making the Southern Ocean one of the largest sources of natural carbon to the atmosphere (Mikaloff-Fletcher et al. 2007). The southerly part of the upwelled CDW flows southward and sinks as Antarctic Bottom Water (AABW)—principally within the subpolar gyres (SPG)—and contributes to the lower MOC cell that ventilates the abyssal ocean. The northerly part flows northward and subducts around the subantarctic front to form Antarctic Intermediate Water (AAIW) and Subantarctic Mode Water (SAMW) and contributes to the upper MOC cell that ventilates the subtropical gyres (STG). Where northward flowing waters of the upper MOC cell converge and subduct with southward flowing surface subtropical waters (SW), the air–sea CO_2 flux is predominately ingassing: strong cooling and biological production make this region a dominant sink of natural CO_2 (Metzl et al. 1999; McNeil et al. 2007). The anthropogenic component tends to oppose the natural component in the upwelling regions of the Southern Ocean, where deep waters with low anthropogenic carbon concentrations are ventilated. This, combined with the impact of strong winds and high CO_2 solubility, makes the Southern Ocean the dominant anthropogenic carbon uptake region—accounting for about 40% of the global ocean uptake (Khatiwala et al. 2009).

Although the processes responsible for historical and future atmospheric CO_2 uptake by the ocean are broadly understood, we are still unable to definitively quantify and ascribe historical air–sea CO_2 fluxes (Frölicher et al. 2015) and carbon cycle feedbacks (Roy et al. 2011) to specific physical and biogeochemical mechanisms in analyses of multiple ESM projections. Critical steps toward improving confidence in long-term projections of Earth's climate include quantifying the key regional processes that drive carbon cycle feedbacks and their contribution to intermodel convergence/divergence in the evolution of projected ocean uptake of CO_2.

The spatial distributions of carbon cycle feedbacks provide valuable information on the potential mechanisms (Boer and Arora 2010; Roy et al. 2011; Ciais et al. 2013). The longitudinally banded spatial distribution of carbon cycle feedbacks parameters in the Southern Ocean are clearly linked to the meridional overturning circulation and the obduction and subduction pathways that ventilate water masses (Séférian et al. 2012), which are, in turn, intrinsically associated with the advection along isopycnal (constant density) surfaces. Therefore, water masses, defined using density coordinates, provide a natural framework to integrate the impacts of the ocean circulation on the air–sea flux and storage of CO_2 (Iudicone et al. 2011).

In previous studies that used water mass frameworks to analyze projected changes in the marine carbon cycle, time-invariant densities were used to define water mass (WM) boundaries (Séférian et al. 2012; Resplandy et al. 2013), which do not track WMs as their densities evolve in response to anthropogenic forcing. In Séférian et al. (2012), WM boundaries were determined by ‘‘eyeballing’’ the distinguishing features of water masses: an effective approach for a single model if changes in the density of the WM boundaries are small (e.g., historical period) but unfeasible for multimodel ensembles of long climate change simulations. Also, subjective water mass criteria cannot be applied consistently, neither across disparate simulations nor by different users. The approach of Sallée et al. (2013b) uses objective criteria based on key features of the water masses and should be a more robust and efficient approach to diagnose the WM boundaries and ensure the salient mechanistic properties of the water masses have been captured.

TABLE 1. Key references for the ESMs used in this study. Please see Arora et al. (2020) for more model details.

Model acronym	Model full name	Key reference
IPSL-CM5A-LR	L'Institut Pierre-Simon Laplace Coupled Model, version 5A, low resolution	Dufresne et al. (2013)
CanESM2	Canadian Earth System Model, version 2	Arora et al. (2011)
HadGEM2-ES	Hadley Centre Global Environment Model, version 2—Earth System	Collins et al. (2011)
BCC_CSM1.1	Beijing Climate Centre, Climate System Model, 1–1	Wu et al. (2013)
MPI-ESM-LR	Max Planck Institute Earth System Model, low resolution	Ilyina et al. (2013)
NorESM1-ME	NorESM1-M with carbon cycling (and biogeochemistry)	Tjiputra et al. (2013)
CNRM-CM5	Centre National de Recherches Météorologiques Coupled Global Climate Model, version 5	Voldoire et al. (2013)
CESM1(BGC)	Community Earth System Model, version 1.0, biogeochemical cycles	Lindsay et al. (2014)

Our goal is to develop an efficient, consistent, and reproducible Southern Ocean water mass tracking procedure to (i) facilitate intermodel and model–data comparisons, (ii) diagnose and quantify the major drivers of carbon cycle feedbacks over water masses in IPCC-class Earth system models, and (iii) investigate mechanisms driving projected changes in air–sea CO_2 fluxes. We aim to demonstrate that water mass frameworks are valuable tools for developing a coherent picture of the processes driving intermodel divergence/convergence in projected Southern Ocean carbon uptake.

In section 2, we present the water mass and carbon cycle feedback frameworks that we use to partition the carbon cycle feedbacks over each water mass: two carbon–concentration feedbacks (dpCO_2 and carbonate buffering capacity) and two carbon–climate feedbacks (outcrop surface area and local climate impacts). In section 3, we present the water mass boundaries and outcrop surface areas diagnosed by the water mass framework. In section 4, the contributions of four carbon cycle feedbacks to the change in the cumulative uptake of atmospheric CO_2 by the Southern Ocean, and each of its constituent water masses, are quantified to identify the dominant feedbacks and sources of intermodel variability, and the feedback sensitivity parameters (β and γ) are analyzed to help interpret the underlying mechanisms.

2. Method

a. Models

We included all ESMs from phase 5 of the Coupled Model Intercomparison Project (CMIP5) (Table 1) for which the required simulations (preindustrial, piControl, and idealized 1% atmospheric CO_2 increase simulations: 1pctCO2 and esmFixClim1, section 2c) and variables (monthly depth-resolved temperature and salinity, monthly air–sea CO_2 fluxes) were available. We focused on the CMIP5 models so that we could draw on a series of papers that comprehensively documented changes in oceanic and atmospheric circulation in the CMIP5 ESMs (Meijers et al. 2012; Bracegirdle et al. 2013; Sallée et al. 2013a,b; Meijers 2014) to help interpret the potential mechanisms responsible for the changes in CO_2 uptake.

b. SO-APT

We developed an automated procedure (SO-APT) for tracking Southern Ocean water masses (SW, SAMW, AAIW, CDW, AABW), based on modifications to the Sallée et al. (2013b) approach. This version has improved stability for tracking changes in WM boundaries in multidecadal simulations. The previous version was too sensitive to localized potential vorticity minima, which created unrealistic fluctuations in the SAMW boundaries.

To diagnose the densities of the WM boundaries, SO-APT exploits characteristic features of annual-mean and zonally averaged (at 30°S) vertical hydrographic profiles in the STGs north of the SAMW subduction zones (Sallée et al. 2010) where the WMs are clearly distinguishable. Vertical profiles of temperature and salinity are mapped from depth to potential density (σ, reference pressure of 2000 dbar) coordinates to limit the mixing of water masses in the zonal averaging step. Potential vorticity (PV) is calculated as $PV = f_c\sigma_z/p_r$, where f_c is the Coriolis parameter, p_r is the reference pressure of 1000 dbar, and σ_z is the vertical density gradient. The notation for the density of a water mass boundary is $\sigma_{\mathrm{lower\_upper}}$, where lower and upper refer to the WMs above and below the boundary, respectively.

The STG is characterized by an intense near-surface stratification maximum (a maximum in potential vorticity, PV_{max}): the permanent thermocline. Above and below the permanent thermocline lie the SW and the SAMW. The SAMW is characterized by a local minimum in stratification. The boundary between the SW and the SAMW was defined using PV_{max}:

$$\sigma_{\mathrm{SW\_SAMW}} = k_1\sigma(\mathrm{PV}_{\mathrm{max}}), \quad \text{where} \quad k_1 = 0.8. \tag{2}$$

Below the SAMW lies the AAIW, which is characterized by a salinity minimum S_{min}. We defined the density envelope of the AAIW layer based on S_{min} and the local salinity maxima lying above and below, $S_{\mathrm{max\_above}}$ and $S_{\mathrm{max\_below}}$:

$$\sigma_{\mathrm{SAMW\_AAIW}} = k_2\sigma(S_{\mathrm{min}}) + k_3\sigma(S_{\mathrm{max\_above}}), \quad \text{where} \quad k_2 = 0.8 \quad \text{and} \quad k_3 = 0.2, \quad \text{and} \tag{3}$$

$$\sigma_{\mathrm{AAIW\_CDW}} = k_4\sigma(S_{\mathrm{min}}) + k_5\sigma(S_{\mathrm{max\_below}}), \quad \text{where} \quad k_4 = 0.8 \quad \text{and} \quad k_5 = 0.2. \tag{4}$$

The AABW is the very well-mixed bottom boundary layer characterized by the PV_{min}. The CDW lies between the AAIW and AABW. The boundary between CDW and AABW was defined based on PV_{mi}:

$$\sigma_{\mathrm{CDW\_AABW}} = \sigma(k_6\mathrm{PV}_{\mathrm{min}}), \quad \text{where} \quad k_6 = 5. \tag{5}$$

Because AABW does not reach the 30°S latitude band in some models, we compute the PV_{min}, as the minimum below 2000 m

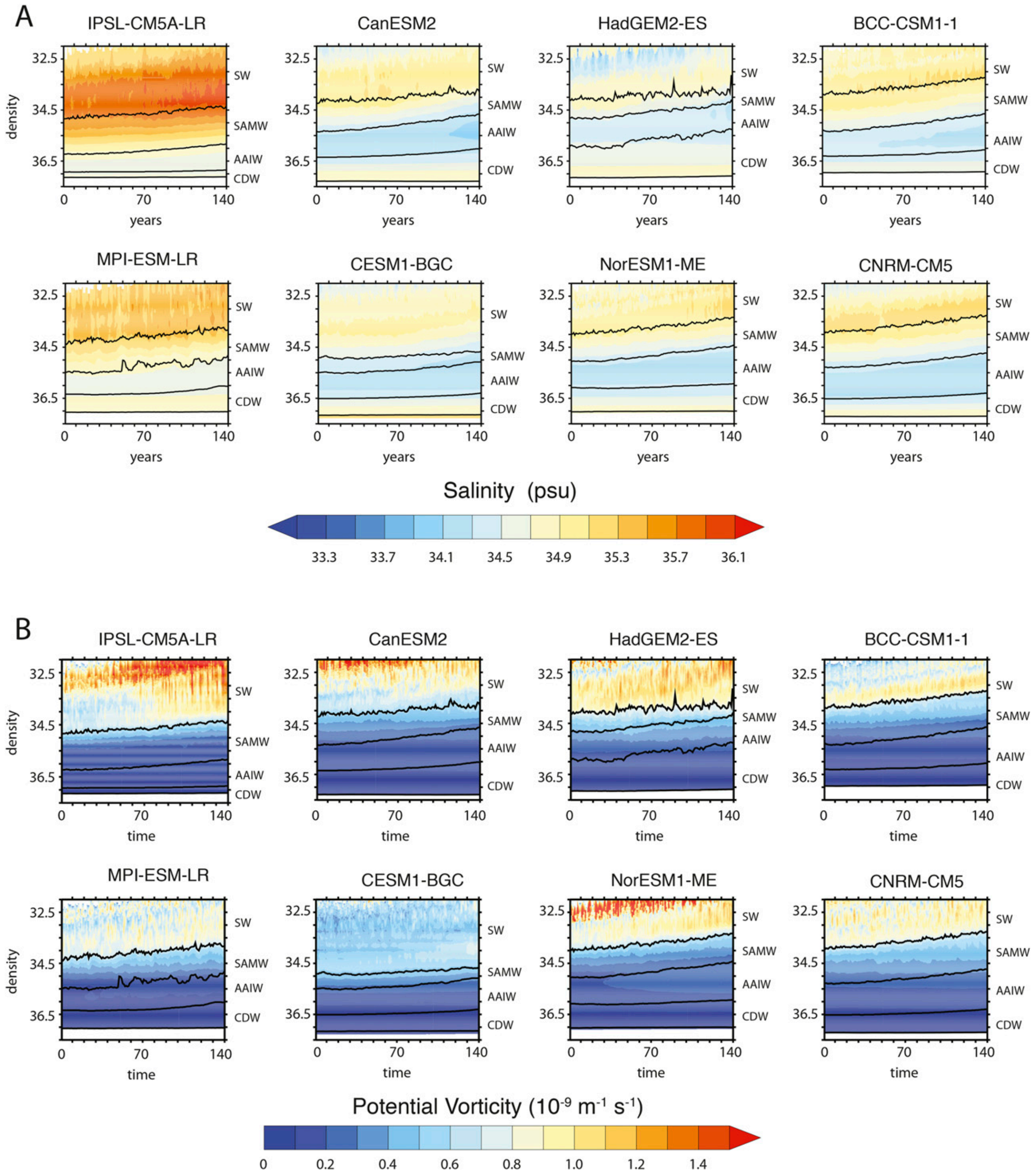

FIG. 1. Time series (140 years from preindustrial conditions) of zonally averaged vertical sections at 30°S of (a) salinity (psu) and (b) PV ($\times 10^{-9}$ m^{-1} s^{-1}) in the CMIP5 ESM 1pctCO$_2$ (COU) simulation. The vertical sections are presented in potential density coordinates (σ; kg m^{-3}) and referenced to 2000 dbar.

south of 50°S. The SO-APT parameters [$k_{[1-7]}$ in Eqs. (2)–(5)] were tuned manually to best capture the WMs across all models used in this study using the climatological average of the first 10 years of the piControl simulations.

Outcrop surface areas of each water mass, $\mathrm{OS}_{\mathrm{wm}}(x, y, t)$, were defined as the ocean surface area, $A(x, y, t)$, enclosed by the winter-averaged (JJA) surface emergence of the lower and upper boundaries of the WMs, σ_{lower} and σ_{upper} [Eqs. (2)–(5)]:

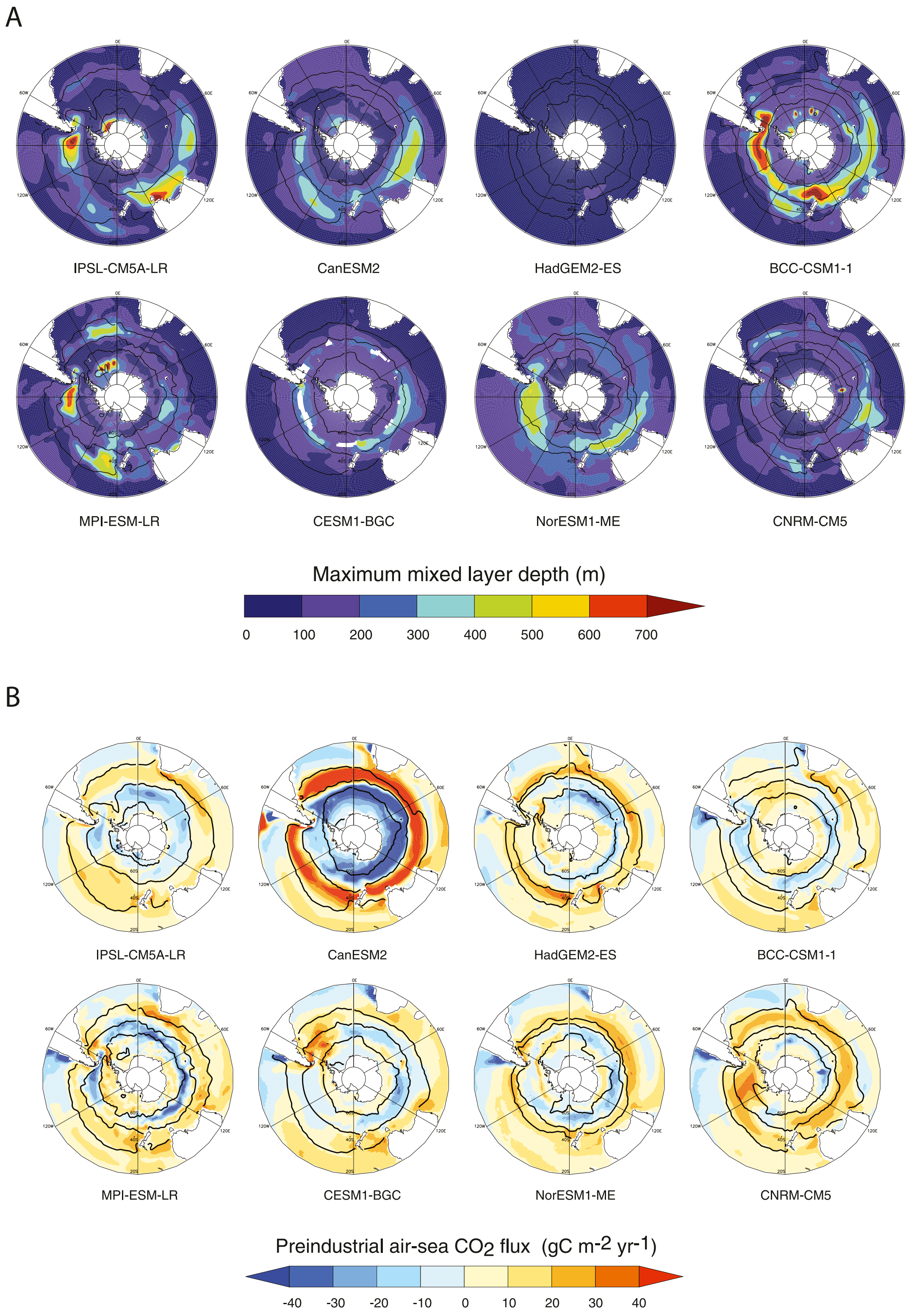

FIG. 2. Spatial distributions of the preindustrial (a) maximum mixed layer depth (m) and (b) annual mean air–sea CO_2 flux f (gC m^{-2} yr^{-1}) in the CMIP5 ESMs, where red shading represents an air–sea CO_2 flux into the ocean and blue shading represents an air–sea CO_2 flux out of the ocean. The preindustrial conditions are represented by the initial conditions (t_0) in the esmFixClim1 simulation. The contours represent the boundaries of the outcrop areas diagnosed using the SO-APT routine.

$$\mathrm{OS}_{\mathrm{wm}}^{\exp}(x,y,t)=A(x,y,t),\quad \begin{cases}\text{for}\quad [x,y,t]\quad \text{where}\quad \sigma_{\mathrm{lower}}(t)<\sigma(x,y,t)<\sigma_{\mathrm{upper}}(t)\\ \mathrm{wm}=[\mathrm{SW},\mathrm{SAMW},\mathrm{AAIW},\mathrm{CDW},\mathrm{AABW}]\end{cases}, \tag{6}$$

where exp represents the model simulation [fully coupled (COU) and biogeochemically coupled (BGC); see section 2c].

Despite the unavoidable compromises when using a common set of objective criteria to diagnose the WM positions across a disparate set of model simulations, we have been encouraged by the efficacy of the SO-APT routine. The AAIW boundaries track the characteristic salinity minimum (Fig. 1a) and the upper boundary of the SAMW tracks the base of the potential vorticity maximum (Fig. 1b) as the boundaries lighten with climate change. Encouragingly, the deep mixed layers in the SAMW and AAIW formation regions (Sallée et al. 2010) largely lie within their WM outcrop areas. The deep mixed layers (MLDs) of the key AAIW formation region near the Drake Passage are located within the boundaries of our AAIW outcrop region for all models (Fig. 2a). Other regions with deeper MLDs (i.e., near the Campbell Plateau, the east Indian, west Pacific) largely lie within the AAIW and SAMW outcrop regions for all models. Also, SO-APT delineates the boundaries between regions with distinct CO_2 flux characteristics: the preindustrial CO_2 flux mostly outgasses in the AAIW and CDW outcrop regions where old deep waters rich in accumulated DIC are obducted to the ocean surface, and ingasses in the subduction regions north of the SAMW–AAIW boundary (Fig. 2b).

c. Carbon cycle feedback framework

We applied a modified version of the Friedlingstein et al. (2006) carbon cycle feedback framework. In Friedlingstein et al. (2006) the cumulative CO_2 emission-driven change in global ocean carbon uptake (ΔC_O) is calculated from CO_2 emission-driven perturbations to the global air–sea CO_2 flux relative to the preindustrial, ΔF ($\mathrm{PgC\,yr^{-1}}$). The ΔC_O (PgC) is partitioned into two components associated with the atmospheric CO_2-driven carbon concentration and climate change–driven carbon–climate feedbacks—ΔCconc (PgC) and ΔCclim (PgC), respectively:

$$\Delta C_O=\int \Delta F\,dt=\Delta C\mathrm{conc}+\Delta C\mathrm{clim}=\beta\Delta \mathrm{pCO_2a}+\gamma\Delta \mathrm{Ta}. \tag{7}$$

The carbon–concentration feedback parameter β ($\mathrm{PgC\,ppm^{-1}}$) represents the sensitivity of the air–sea CO_2 flux per unit change in the globally averaged partial pressure of atmospheric CO_2, $\mathrm{pCO_2a}$ (ppm). The carbon–climate feedback sensitivity parameter γ ($\mathrm{PgC\,K^{-1}}$) represents the sensitivity of the air–sea CO_2 flux per unit change in the globally averaged surface atmospheric temperature (ΔTa; K), which is used as a proxy of climate change.

To partition ΔCconc and ΔCclim we used a pair of idealized climate change simulations that were specifically designed for this purpose (1pctCO_2 and esmFixClim1, Fig. 3). In both simulations the global atmospheric CO_2 concentration increases annually by 1% to 4 times the preindustrial concentration by the end of the 140-yr simulation (Taylor et al. 2012) and biogeochemical processes over land and ocean respond directly to the changing atmospheric CO_2 concentration (biogeochemically coupled). In the standard 1pctCO_2 simulation the radiative forcing is switched on (radiatively coupled), while in the esmFixClim1 simulation it is switched off. Consequently, the increase in atmospheric CO_2 induces climate change in the 1pctCO_2 simulation and not in the esmFixClim1 simulation. In feedback analyses, these simulations are typically referred to as COU and BGC simulations, respectively. In the BGC simulation, CO_2-driven changes to the terrestrial vegetation perturb land–atmosphere water and energy exchanges and induce a small increase in the global temperature. Since the increase in global temperature in the BGC simulation is small (~0.3°C) relative to the COU simulation (~4.8°C), it is assumed negligible to simplify the partitioning of the carbon cycle feedbacks (Arora et al. 2013).

Here we apply a regionalization of the Friedlingstein et al. (2006) approach (Roy et al. 2011) to specifically address carbon cycle feedbacks in the Southern Ocean and complement the global CMIP5 analyses (Arora et al. 2013; 2020). The projected cumulative change in CO_2 uptake by the Southern Ocean south of 20°S (ΔC_{SO}) and its constituent water masses (ΔC_{wm}) are calculated based on the perturbations to the spatial distribution of the net air–sea CO_2 flux relative to the preindustrial period (t_0), $\Delta f(x, y, t)$ ($\mathrm{gC\,m^{-2}\,yr^{-1}}$), where

$$\Delta f^{\exp}(x,y,t)=f^{\exp}(x,y,t)-f^{\exp}(x,y,t_0) \tag{8}$$

and spatially integrating and cumulating Δf over the full simulation (140 years). Here, negative Δf signifies less atmospheric CO_2 uptake by the ocean:

$$\begin{aligned}\Delta C_{\mathrm{SO}}&=\iiint \Delta f^{\exp}(x,y,t)\,dx\,dy\,dt,\quad \text{for}\quad [x,y]\ \text{south of }20°\mathrm{S}\\ &=\Delta C\mathrm{conc}+\Delta C\mathrm{clim}=\beta\Delta \mathrm{pCO_2a}+\gamma\Delta \mathrm{Ta},\end{aligned} \tag{9}$$

and the surface outcrop area [Eq. (6)] of each water masses:

$$\Delta C_{\mathrm{wm}}=\iiint \Delta f^{\exp}(x,y,t)\,dx\,dy\,dt\quad \begin{cases}\text{for}\quad [x,y,t]\quad \text{where}\quad \mathrm{OS}_{\mathrm{wm}}(x,y,t)\\ \mathrm{wm}=[\mathrm{SW},\mathrm{SAMW},\mathrm{AAIW},\mathrm{CDW},\mathrm{AABW}]\end{cases}, \tag{10}$$

where exp represents the simulation (i.e., COU and BGC).

We further extend the approach of Friedlingstein et al. (2006) to partition ΔC_{SO} and ΔC_{WM} into four—rather than

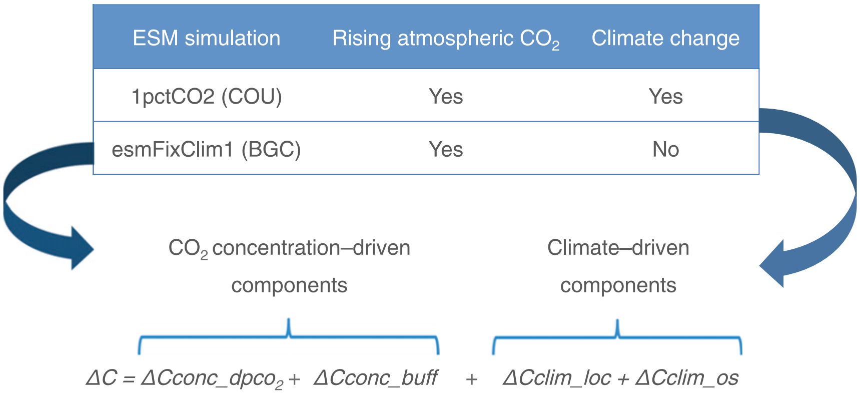

ESM simulation	Rising atmospheric CO_2	Climate change
1pctCO2 (COU)	Yes	Yes
esmFixClim1 (BGC)	Yes	No

FIG. 3. The idealized CMIP5 1% atmospheric CO_2 increase simulations used to diagnose the change in cumulative atmospheric CO_2 uptake (ΔC) associated with carbon cycle feedbacks in the ESMs in the SO: two CO_2-concentration-driven components associated with the carbon–concentration feedback: air–sea dpCO_2 (ΔCconc_dpco2) and carbonate buffering capacity (ΔCconc_buff) and two climate-driven components associated with the carbon–climate feedback: outcrop surface area (ΔCclim_os) and local climate impacts (ΔCclim_loc).

two—feedback components. The ΔCconc component is partitioned into two components: one associated with the increasing dpCO_2 (ΔCconc_dpco2) and one associated with the reduction in the carbonate buffering capacity (ΔCconc_buff). The ΔCclim component is partitioned into two components: one associated with changes in the outcrop surface area (ΔCclim_os) and one associated with local (within water mass) climate change impacts (ΔCclim_loc):

$$\Delta C_{\rm SO}(\text{or } \Delta C_{\rm wm}) = \overbrace{\Delta C\text{conc\_dpco2} + \Delta C\text{conc\_buff}}^{\Delta C\text{conc}} + \overbrace{\Delta C\text{clim\_os} + \Delta C\text{clim\_loc}}^{\Delta C\text{clim}}. \tag{11}$$

For each feedback component (comp) the Δf is denoted Δfcomp; the spatially averaged Δf over a WM, $\overline{\Delta f\text{comp}}_{\rm wm}$ ($\text{gC}\,\text{m}^{-2}\,\text{yr}^{-1}$), is

$$\overline{\Delta f\text{comp}}_{\rm wm}(t) = \frac{\iint \Delta f\text{comp}_{\rm wm}(x,y,t)\,dx\,dy}{\iint \text{OS}_{\rm wm}(x,y,t)\,dx\,dy}, \quad \text{for} \quad [x,y] \quad \text{where} \quad \text{OS}^{\rm exp}_{\rm wm}(x,y,t), \tag{12}$$

and the cumulative and spatially integrated change in CO_2 uptake, $\Delta C\text{comp}_{\rm wm}$ (PgC) is

$$\Delta C\text{comp}_{\rm wm} = \iiint \Delta f\text{comp}_{\rm wm}(x,y,t)\,dx\,dy\,dt, \quad \text{for} \quad [x,y] \quad \text{where} \quad \text{OS}^{\rm exp}_{\rm wm}(x,y,t). \tag{13}$$

1) CARBON–CONCENTRATION FEEDBACK (β) COMPONENTS (ΔCCONC, ΔCCONC_DPCO2, ΔCCONC_BUFF)

The ΔCconc feedback component is diagnosed using the BGC simulation, where the perturbation to Δf is assumed to be due to ΔpCO_2a alone and Eq. (9) simplifies to

$$\Delta C^{\rm BGC} \approx \Delta C\text{conc} \approx \iiint \Delta f^{\rm BGC}(x,y,t)\,dx\,dy\,dt \approx \beta(t)\Delta \text{pCO}_2\text{a}(t). \tag{14}$$

The spatially resolved Δf associated with β, Δfconc, is

$$\Delta f\text{conc}(x,y,t) \approx \Delta f^{\rm BGC}(x,y,t), \tag{15}$$

and the cumulative, spatially integrated Δf associated with β over the SO or its WMs, $\Delta C\text{conc}_{\rm wm}$, is

$$\Delta C\text{conc}_{\rm wm} = \iiint \Delta f\text{conc}_{\rm wm}(x,y,t)\,dx\,dy\,dt \quad \text{for} \quad [x,y] \quad \text{where} \quad \text{OS}^{\rm BGC}_{\rm wm}(x,y,t). \tag{16}$$

The spatial distribution of β, $\beta_{\rm spatial}$, is

$$\beta_{\rm spatial}(x,y,t) = \frac{\int \Delta f\text{conc}(x,y,t)\,dt}{\Delta \text{pCO}_2\text{a}(t)}, \tag{17}$$

and the WM-averaged β, $\beta_{\rm wm}$ ($\text{gC}\,\text{m}^{-2}\,\text{ppm}^{-1}$), is

$$\beta_{\rm wm}(t) = \frac{\int \overline{\Delta f\text{conc}}_{\rm wm}(t)\,dt}{\Delta \text{pCO}_2\text{a}(t)}. \tag{18}$$

To partition ΔCconc for each WM into two components [ΔCconc_buff and ΔCconc_dpCO_2, Eq. (11)], we use a simple heuristic approach based on the temporal evolution of β (Fig. 4), which is set by the relative influence of increasing dpCO_2 (i.e., disequilibrium) and diminishing carbonate buffering capacity on the air–sea CO_2 flux (Katavouta and Williams 2021). Initially the dpCO_2 effect dominates: CO_2 accumulates faster in the atmosphere than in the ocean causing a rapid initial increase in dpCO_2 and $\beta(t)$ (Fig. 4). As the ocean accumulates anthropogenic DIC, partial equilibration and the reduction in the buffering capacity contribute to the tapering off of $\beta(t)$. In water masses that are continuously replenished by low anthropogenic DIC waters (e.g., CDW), the rate of increase in dpCO$_2$ continues to accelerate and $\beta(t)$ tapers off later than in more recently ventilated waters (e.g., SAMW) where the reemergence of anthropogenic DIC dampens the rate of increase of dpCO$_2$. The turning point $t_{\max}$ (Fig. 4) represents where the decrease in the buffering capacity dominates over the increase in dpCO$_2$ and causes $\beta(t)$ to decrease. We estimate ΔCconc_buff based on the decrease in $\beta(t)$ after $t_{\max}$ (Fig. 4). Although, this approach clearly underestimates the impact of the decreasing buffer capacity on carbon uptake, the purpose here is to develop a sense of the magnitude and spatiotemporal variability of this feedback relative to others in the system. Based on this approach, the cumulative, water mass–averaged Δfconc_buff and Δfconc_dpco2 are

$$\int \overline{\Delta f\text{conc\_buff}}_{\text{wm}}(t)\,dt = \left\{\begin{array}{ll} 0, & \text{for} \quad t \le t_{\max} \\ [\overline{\beta}_{\text{wm}}(t) - \overline{\beta}_{\text{wm}}(t_{\max})] \times \Delta\text{pCO}_2\text{a}(t), & \text{for} \quad t > t_{\max} \end{array}\right\}$$

$$\int \overline{\Delta f\text{conc\_dpco2}}_{\text{wm}}(t)\,dt = \left\{\begin{array}{ll} [\overline{\beta}_{\text{wm}}(t)] \times \Delta\text{pCO}_2\text{a}(t), & \text{for} \quad t \le t_{\max} \\ [\overline{\beta}_{\text{wm}}(t_{\max})] \times \Delta\text{pCO}_2\text{a}(t), & \text{for} \quad t > t_{\max} \end{array}\right\}, \tag{19}$$

where

$$\beta\text{max}_{\text{wm}}(t_{\max}) = \max_{t=1:140}[\beta_{\text{wm}}(t)], \tag{20}$$

and $\beta_{\text{wm}}(t)$ was smoothed using a 10-yr running mean to minimize the influence of interannual variability on the estimate of $t_{\max}$.

The cumulative, spatially integrated Δf associated with the two carbon–concentration feedbacks are

$$\Delta C\text{conc\_buff}_{\text{wm}} = \int \overline{\Delta f\text{conc\_buff}}_{\text{wm}}(t) \iint \text{OS}_{\text{wm}}(x, y, t)\,dx\,dy\,dt$$

$$\Delta C\text{conc\_dpco2}_{\text{wm}} = \int \overline{\Delta f\text{conc\_dpco2}}_{\text{wm}}(t) \iint x\text{OS}_{\text{wm}}(x, y, t)\,dx\,dy\,dt. \tag{21}$$

To assess the relative strengths of the changes in buffering capacity between WMs and between models, we defined a buffering sensitivity parameter ϕ_{wm} (gC m^{-2} ppm^{-1})

$$\phi_{\text{wm}} = \frac{\int \overline{f\text{conc\_buff}}_{\text{wm}}(t)\,dt}{\Delta p\text{CO}_2 a}. \tag{22}$$

2) Carbon–climate feedback (γ) components (ΔCclim, ΔCclim_os, ΔCclim_loc)

The cumulative change in CO$_2$ uptake associated with γ, ΔCclim, is estimated from the difference between the COU and BGC simulations. Equation (9) rearranges and simplifies to

$$\begin{aligned} \Delta C\text{clim} &\approx \Delta C^{\text{COU}} - \Delta C^{\text{BGC}} \\ &\approx \iiint \Delta f^{\text{COU}}(x, y, t)\,dx\,dy\,dt - \iiint \Delta f^{\text{BGC}}(x, y, t)\,dx\,dy\,dt \\ &\approx \iiint \Delta f\text{clim}(x, y, t)\,dx\,dy\,dt = \gamma(t)\Delta\text{Ta}(t). \end{aligned} \tag{23}$$

The spatially resolved Δf associated with γ, Δfclim, is

$$\Delta f\text{clim}(x, y, t) \approx \Delta f^{\text{COU}}(x, y, t) - \Delta f^{\text{BGC}}(x, y, t). \tag{24}$$

The spatial distribution of γ, γ_{spatial} (gC m^{-2} K^{-1}), is

$$\gamma_{\text{spatial}}(x, y, t) = \frac{\int \Delta f\text{clim}(x, y, t)\,dt}{\Delta\text{Ta}(t)}. \tag{25}$$

Because the positions of the WMs differ between the COU and BGC simulations, ΔCclim and γ associated with each WM could not be calculated by simple subtraction over geographical coordinates. Therefore, we partitioned ΔCclim for each WM into the two components: ΔCclim_loc and ΔCclim_os [Eq. (11)].

We estimated the ΔCclim_loc based on Δfclim_loc, the spatially resolved Δfclim inside the WM outcrop area common to COU and BGC simulations, that is, $\text{OS}_{\text{wm}}^{\text{COU}}(x, y) \cap \text{OS}_{\text{wm}}^{\text{BGC}}(x, y)$:

$$\Delta f\text{clim\_loc}_{\text{wm}}(x, y, t) = \Delta f\text{clim}_{\text{wm}}(x, y, t), \quad \text{where } \text{OS}_{\text{wm}}^{\text{COU}}(x, y) \cap \text{OS}_{\text{wm}}^{\text{BGC}}(x, y). \tag{26}$$

The spatially resolved Δfclim_os component, is the Δfclim distribution due to WM expansion, Δfclim_$^{+}$os—where the locations where a WM outcrops in the COU simulation but not in the BGC simulation, that is $\text{OS}_{\text{wm}}^{\text{COU}}(x, y, t) \backslash \text{OS}_{\text{wm}}^{\text{BGC}}(x, y, t)$, such that

$$\Delta f\text{clim\_}^{+}\text{os}_{\text{wm}}(x, y, t) = \Delta f_{\text{wm}}^{\text{COU}}(x, y, t), \quad \text{where} \quad \text{OS}_{\text{wm}}^{\text{COU}}(x, y, t) \backslash \text{OS}_{\text{wm}}^{\text{BGC}}(x, y, t), \tag{27}$$

and WM contraction, Δfclim_$^{-}$os,

$$\Delta f\text{clim\_}^{-}\text{os}_{\text{wm}}(x, y, t) = \Delta f_{\text{wm}}^{\text{BGC}}(x, y, t), \quad \text{where} \quad \text{OS}_{\text{wm}}^{\text{BGC}}(x, y, t) \backslash \text{OS}_{\text{wm}}^{\text{COU}}(x, y, t), \tag{28}$$

such that

$$\Delta f\text{clim\_os}_{\text{wm}}(x,y,t) = \Delta f\text{clim\_}^{+}\text{os}(x,y,t) + \Delta f\text{clim\_}^{-}\text{os}(x,y,t)\,, \tag{29}$$

The cumulative, spatially integrated Δf associated with the two carbon–climate feedbacks are

$$\begin{aligned}\Delta C\text{clim\_loc}_{\text{wm}}(t) &= \iiint \Delta f\text{clim\_loc}_{\text{wm}}(x,y,t)\,dx\,dy\,dt\\ \Delta C\text{clim\_os}_{\text{wm}}(t) &= \iiint \Delta f\text{clim\_}^{+}\text{os}_{\text{wm}}(x,y,t)\,dx\,dy\,dt + \iiint \Delta f\text{clim\_}^{-}\text{os}_{\text{wm}}(x,y,t)\,dx\,dy\,dt.\end{aligned} \tag{30}$$

The average γ for each WM, γ_{wm} ($\text{gC}\,\text{m}^{-2}\,\text{K}^{-1}$), is

$$\gamma_{\text{wm}}(t) = \frac{\int \overline{\Delta f\text{clim\_loc}}_{\text{wm}}(t)\,dt}{\Delta\text{Ta}(t)}. \tag{31}$$

3. Diagnosis of water mass boundaries and outcrop surface areas

SO-APT efficiently locates and tracks the boundaries (Fig. 1 and S1 in the online supplemental material) and outcrops (Fig. 2) of the key WMs in the Southern Ocean in a multimodel ensemble of climate projections. The positions of the outcrop areas of each water mass differ widely between the models (Fig. 2), confirming that studies that use fixed geographical regions mix water masses with distinctly different circulation and carbon cycle characteristics—and in different proportions—making diagnosis and interpretation of the carbon cycle feedbacks challenging.

There is a large spread (>1 $\text{kg}\,\text{m}^{-3}$) in the initial potential densities of the WM boundaries in the CMIP5 models (Fig. 5a). The densities of the WM boundaries lighten by up to 0.7 $\text{kg}\,\text{m}^{-3}$ by year 2100 (Fig. 5b). The reduction in density is strongest at the SAMW and AAIW boundaries, which has been attributed to warming and freshening over the ocean surface based on both observations (Bindoff and McDougall 2000; Hobbs et al. 2021) and climate change projections (Downes et al. 2009; Sallée et al. 2013b). The large intermodel variability in the densities of the water mass boundaries (Fig. 1) and their evolution (Fig. 5), re-emphasizes that using common or temporally fixed densities to define WM boundaries would not accurately capture the defining characteristics and position of WMs in a disparate ensemble of models.

A comparison of observed and simulated WM boundaries shows the largest biases are in the density of AAIW–SAMW boundaries, which tend to be lighter than observed (Fig. 5a) and can be explained by pervasive warm biases (Sallée et al. 2013b). The IPSL-CM5A-LR model consistently has the reverse bias: all boundaries except the AABW–CDW boundary are too dense and can be explained by salty biases in the SWs, SAMWs, and AAIWs (Fig. 1a and Sallée et al. 2013b).

Similarly, there is substantial intermodel variability in the representation of both the preindustrial and the projected outcrop areas of the WMs (Figs. 5c,d) and systematic biases in the outcrop areas (Figs. 5c and 7b). For the lighter water masses: in most models the SW outcrop areas are too small compared to an observation-based estimate (~75% for the multimodel median), while the SAMW and AAIW outcrop areas are too large (by ~40% and ~70% for the multimodel median).

The SW outcrop area is associated with the representation of the STGs. In the CMIP5 models the SW outcrop areas are too small because the STGs are positioned too far north and can be explained by the strength and position of the wind stress and wind stress curl maxima, which are biased too strong and too far equatorward (Meijers et al. 2012). Conversely, in the one model that has a larger than observed SW outcrop area (NorESM1-ME, Fig. 5c), the maxima of the STG strength and the wind stress curl are positioned further poleward relative to most other CMIP5 models (Meijers et al. 2012). The outcrop area of the SAMWs and AAIWs is associated with the position of the STGs from the north and the position of the ACC from the south. Since the position of the Antarctic Circumpolar Current (ACC) is captured relatively well in CMIP5 models (Meijers et al. 2012), we expect the SAMWs and AAIWs outcrops areas are too large due to the northward bias of the STG position.

We expect the large intermodel variability in the SAMW outcrop area is related to the variable representation of maximum mixed layer depths in the eastern Indian and Pacific Oceans where strong subduction of SAMWs occur (Fig. 12 in Sallée et al. 2013b). The intermodel variability in the magnitude of the CDW outcrop area should be strongly associated with the extent of the SPGs and the latitude of the southern boundary of the ACC, which both vary widely between CMIP5 models (Meijers et al. 2012).

4. Diagnosis of carbon cycle feedbacks

a. *Carbon–concentration feedbacks (β and ΔCconc)*

The carbon–concentration feedback is overwhelmingly positive over the Southern Ocean (Fig. 6): dpCO_2 increases with rising atmospheric CO_2, driving more CO_2 into the ocean relative to preindustrial conditions. The magnitude of β (the change in CO_2 uptake per unit increase in atmospheric CO_2) peaks in the circumpolar upwelling band where the deep waters of the global ocean with low anthropogenic DIC are ventilated and CO_2 uptake is efficient (Fig. 6a). The β maxima vary in position and intensity between the models (Figs. 6b,c).

1) DpCO$_2$ FEEDBACK (ΔCCONC_DPCO$_2$)

Rising dpCO_2 increases the multimodel cumulative (140 yr) change in Southern Ocean CO_2 uptake ($\Delta C\text{conc\_dpCO}_2$) by

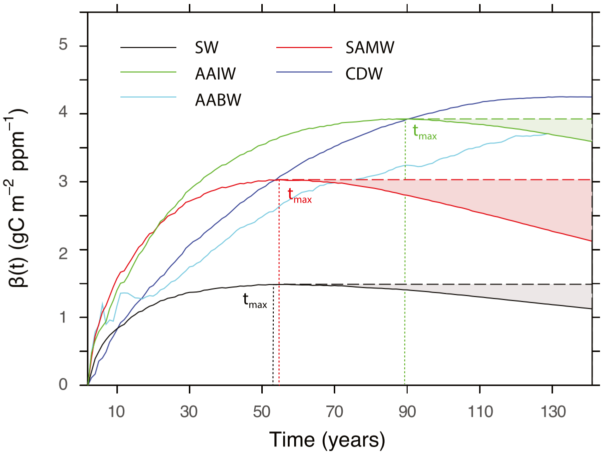

FIG. 4. The evolution of multimodel mean $\beta(t)$ over SO water masses. The turning point t_{max} represents the time when the reduction in buffering capacity dominates the evolution of $\beta(t)$. The dashed lines represent the upper limit of the approximation used to estimate the minimum cumulative change in CO_2 uptake associated with the reduction in buffer capacity, ΔCconc_buff (shaded areas).

326 PgC [interquartile range (IQR): 90 PgC, Fig. 7a, Table 2]. Even though β is stronger in the CDW (Fig. 6b), AAIW contributes most to ΔCconc_dpCO_2 (106 PgC, Fig. 7a)—due to its vast circumpolar distribution, largely uninterrupted by land and sea ice. Consequently, the large intermodel variability of β in the AAIW outcrop area strongly impacts the net Southern Ocean carbon uptake: models with lower β (Fig. 6b) and ΔCconc_dpCO_2 in the AAIWs [CanESM2, HadGEM2-ES, CESM1(BGC), CNRM-CM5] tend to have lower Southern Ocean CO_2 uptake (ΔCconc_dpCO_2, Fig. 7a) than models with higher β and ΔCconc_dpCO_2 in the AAIWs (IPSL-CM5A-LR and MPI-ESM-LR).

The large intermodel variability in ΔCconc_dpCO2 in AAIWs and CDWs (IQRs of 43 and 58 PgC, respectively; Table 2) is mostly associated with the large intermodel variability in β (Fig. 6b). For the CDWs, it is also modulated by variability in their outcrop areas (Fig. 5c), which we expect is partly related to the variable extent of the subpolar gyres (Fig. 7b, section 3).

The magnitude of β and the CO_2 uptake capacity of the Southern Ocean are most likely associated with water mass formation/destruction rates in the net upwelling regions (CDW and AAIW). A cursory comparison of the intermodel variability in β (Fig. 6b) and surface water mass formation rates (Fig. 7 in Sallée et al. 2013b) supports this relationship: in the AAIW outcrop areas, models such as IPSL-CM5A-LR and MPI-ESM-LR have the strongest obduction rate (i.e., water mass consumption; Sallée et al. 2013b) and β values; conversely, models such as CNRM-CM5 and HadGEM2-ES have comparatively very weak obduction or subduction rates (Sallée et al. 2013b) and low β values. We find a similar relationship in the CDW: here HadGEM2-ES has a strong obduction rate (Sallée et al. 2013b) and high β, while IPSL-CM5A-LR has a very weak obduction rate (Sallée et al. 2013b) and low β. In future, we recommend using the same WM framework for the water mass circulation and carbon cycle feedback analysis to elucidate this relationship.

The high intermodel variability of β in AAIWs is most likely due to the variable representation of subduction/obduction in this region. Sallée et al. (2013b) showed that most models obduct within the CDW density range and subduct within the SAMW density range: and, although the AAIW tend to be a net obduction region (Fig. 7b), subduction/obduction is more variable in the AAIW density range. More work is needed to identify the mechanisms responsible for the intermodel variability in water mass formation/destruction here.

The position of the band of maximum upwelling also leads to variations in Southern Ocean CO_2 uptake. For example, the obduction (Fig. 7 in Sallée et al. 2013b) and β in HadGEM2-ES is relatively strong but positioned further poleward (Fig. 7c) restricting the total area for obduction and leading to lower CO_2 uptake relative to other models with similar obduction strengths (i.e., IPSL-CM5A-LR and MPI-ESM-LR).

Given the apparent sensitivity of the dpCO_2 feedback to the strength and position of obduction and subduction pathways, circulation diagnostics such as water mass formation, transformation, and export could be effective mechanistic constraints on the future CO_2 uptake by the Southern Ocean: but there are limited observations at the scale of specific water masses. Interior transports across 30°S (Russell et al. 2018) and emergent circulation properties, such as water mass outcrop areas and volumes could be effective alternatives.

2) CARBONATE BUFFERING CAPACITY FEEDBACK (ΔCCONC_BUFF)

The reduction in the buffering capacity reduces the multimodel cumulative (140 yr) change in CO_2 uptake (ΔCconc_buff) by −49 PgC (IQR: 13 PgC, Fig. 7a and Table 2). An unequivocal reduction (up to 30%) in the ocean CO_2 uptake capacity occurs after ~50 years in SW and SAMW (Fig. 8a), and significantly later in AAIW (~90 yr) and CDW (~120 yr). The largest reduction occurs in the SAMW (−28 PgC, Fig. 7b, Table 2), in agreement with trends from recent observational studies (Salt et al. 2015). For the majority of models, the CO_2 saturation sensitivity ϕ is strongest in the SAMW (Fig. 8b). Although the ϕ of SW is weaker, the outcrop area of the SW is large (Fig. 5c,d), making the SW the second largest contributor to buffer feedback. Together, SAMWs and SWs are responsible for about 90% of the buffer-driven reduction in CO_2 uptake (Fig. 7a). A more precise diagnostic of the impact of the buffering capacity on carbon uptake [see methods in section 2c(1)] would increase the estimate of ΔCconc_buff, making it an even more important contributor to the Southern Ocean carbon cycle feedback.

We expect the differences in the carbonate saturation sensitivity of the water masses are largely related to DIC accumulation rates. First, SW and SAMW have higher initial buffer capacities than AAIW and CDWs, which is related to their lower DIC to alkalinity ratios (DIC/ALK; Sabine et al. 2002). By definition, for the same increase in atmospheric CO_2, waters with higher buffer capacities can take up more carbon than waters with lower buffer capacities, which can result in faster

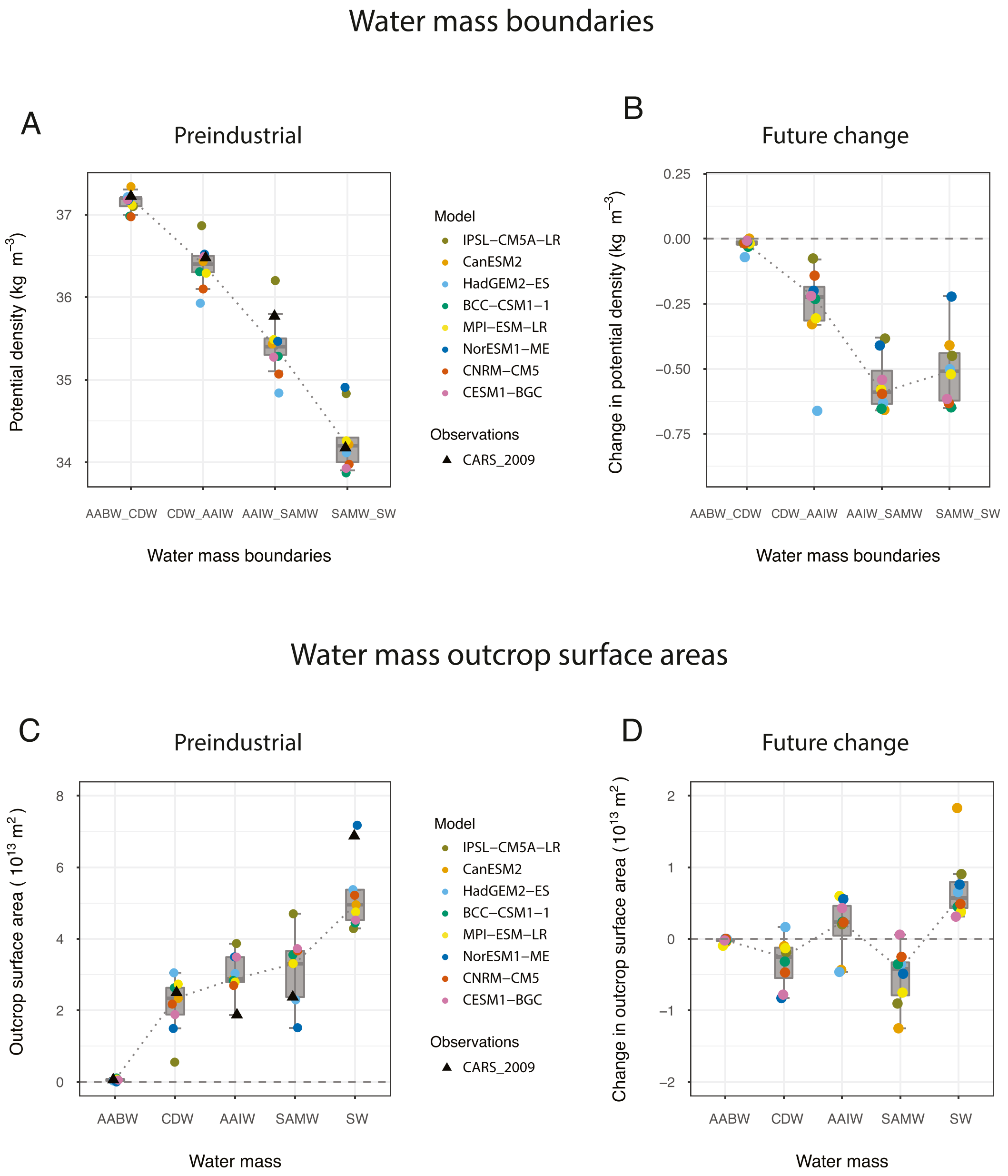

FIG. 5. Potential density (σ) of SO water mass boundaries in the CMIP5 models diagnosed using the SO-APT procedure: (a) preindustrial (t_0) and (b) future change ($t_{140} - t_0$). Outcrop surface area (OS) of SO water masses: (c) preindustrial and (d) future change ($t_{140} - t_0$). Colored circles represent results from the individual CMIP5 models and black triangles represent the results based on observed fields from the CSIRO Atlas of Regional Seas (Ridgway et al. 2002). The multimodel median is shown by a vertical line, the box represents the IQR and the whiskers the 5th–95th percentile limits. Note that although the simulations used here do not have a historical period, the historical change is relatively small compared to the future perturbation (Frölicher et al. 2015), so a comparison between the preindustrial conditions and observations is informative.

increases in DIC/ALK and faster reductions in their buffer capacities (Egleston et al. 2010) and the subsequent CO_2 uptake. Second, faster DIC accumulation is expected in SAMW and SWs relative to AAIW and CDW because they have higher surface area to volume ratios (Séférian et al. 2012; Resplandy et al. 2013). Third, the recirculation and reemergence of anthropogenic DIC and ALK to the ocean surface via across-WM (diapycnal) exchange and along-isopycnal transport and diffusion also contributes to the rate of DIC accumulation. Based on global model studies, a significant proportion of water mass volume (Sallée et al. 2013b) and carbon (Iudicone et al. 2016) are transferred from SWs to denser SAMWs and AAIWs within the ocean interior (Fig. 7b). Subtropical cells are effectively flushing out the

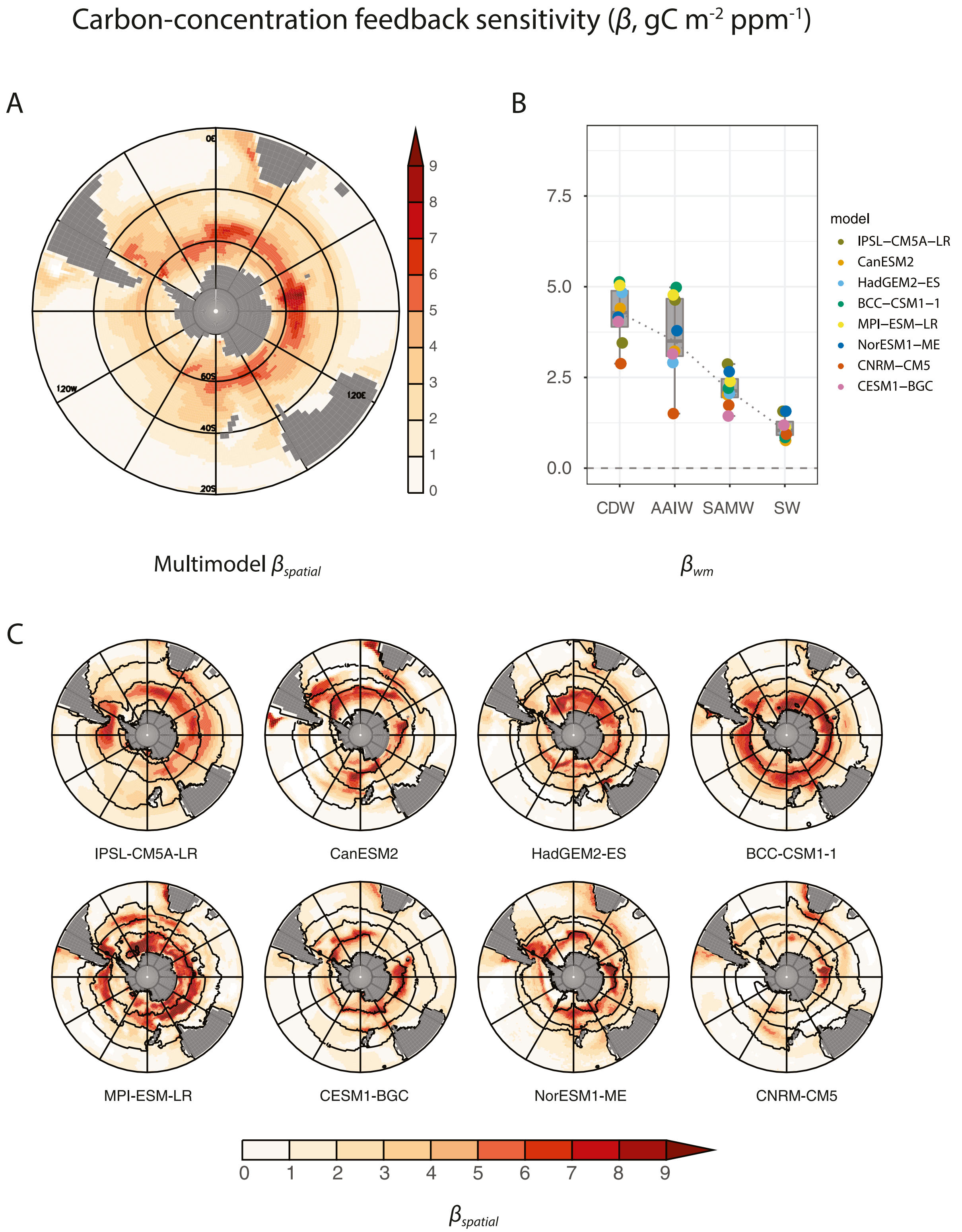

FIG. 6. SO carbon–concentration feedback sensitivity parameters β (gC m^{-2} ppm^{-1}) in the CMIP5 ESMs: (a) Multimodel-mean spatially resolved β, β_{spatial}; (b) water mass–averaged β, β_{wm}. The horizontal gray line, box, and whiskers represent the multimodel median, the IQR, and the 5th–95th percentile limits, respectively. (c) Spatially resolved β, β_{spatial}, for each CMIP5 model. The contours represent the boundaries of the SO outcrop surface areas, OS. The β_{wm} of each model and SO water mass are tabulated in supplementary material S3.

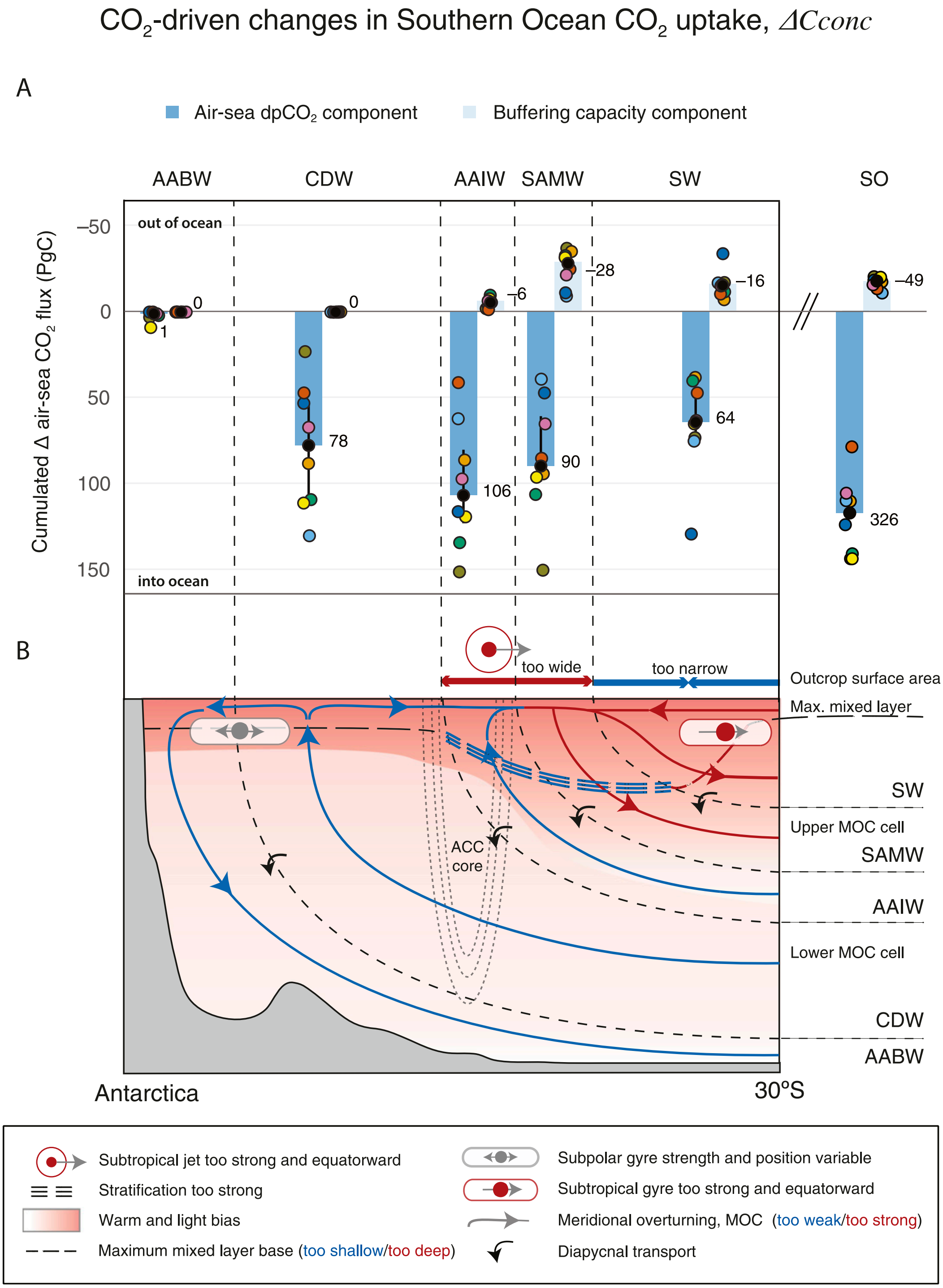

FIG. 7. The cumulated change in the air–sea CO$_2$ flux (Δ*C*conc, PgC) and the ocean circulation mechanisms potentially associated with carbon–concentration feedback (β). (a) The two components of Δ*C*conc over the SO and each of its water masses: (i) Δ*C*conc_dpCO$_2$ (dark blue)—the component driven by air–sea CO$_2$ partial pressure difference, dpCO$_2$, and (ii) Δ*C*conc_buff (light blue)—the component driven by the reduction in the buffering capacity. Note these are the same quantities and color schemes used in the summary Fig. 10. The multimodel median and IQR are represented by the filled black circle and whiskers, respectively. Colored circles represent the individual CMIP5 models (see Fig. 4 for the CMIP5 model key). Positive values signify more ocean uptake of atmospheric CO$_2$. (b) Schematic of the major biases in the CMIP5 multimodel ocean circulation (Meijers et al. 2012; Bracegirdle et al. 2013; Sallée et al. 2013a,b; Meijers 2014) that are expected to contribute to the carbon–concentration feedback.

TABLE 2. The atmospheric CO_2-driven (ΔCconc_dpco2 and ΔCconc_buff; PgC) contributions to the cumulative (140 yr) change in atmospheric CO_2 uptake over the SO south of 20°S (ΔCso; PgC) and each of the major SO water masses for each ESM used in this study.

	ΔCconc_dpco2						ΔCconc_buff						ΔCconc
Model	SW	SAMW	AAIW	CDW	AABW	SO	SW	SAMW	AAIW	CDW	AABW	SO	SO
IPSL-CM5A-LR	73	150	151	23	3	400	−17	−37	−2	0	0	−56	344
CanESM2	38	94	86	88	1	307	−7	−35	−5	0	0	−48	259
HadGEM2-ES	75	39	62	130	1	306	−17	−9	−4	0	0	−30	276
BCC_CSM1.1	40	106	134	109	2	392	−12	−33	−10	0	0	−54	337
MPI-ESM-LR	65	96	119	111	9	400	−16	−32	−8	0	0	−55	345
NorESM1-ME	129	47	116	53	0	345	−34	−11	−6	0	0	−51	294
CNRM-CM5	47	85	41	47	0	219	−10	−25	−1	0	0	−37	183
CESM1(BGC)	63	65	97	67	1	294	−15	−22	−7	0	0	−43	251
Median	64	89	106	78	1	326	−16	−28	−6	0	0	−49	285
IQR	28	38	43	58	2	90	6	14	4	0	0	13	82

anthropogenic CO_2 from SWs, enabling SWs to continue taking up CO_2 (Nakano et al. 2015). Conversely, SAMWs are accumulating anthropogenic CO_2 from both the subtropical cells and the upper branch of the MOC, which also accelerates the rate of accumulation of DIC and the reduction of the buffering capacity here. By contrast, even though CDW have lower initial buffer capacities, they are replenished by old waters with low anthropogenic CO_2 concentrations, which limits the rate of DIC accumulation and fast changes in the buffer capacity here.

b. Carbon–climate feedbacks (γ and ΔCclim)

The multimodel mean distribution of γ (the change in CO_2 uptake per unit increase in atmospheric temperature) is characterized by a striking longitudinally banded structure of alternating sign (Fig. 9a): the γ in AAIWs and SWs are negative

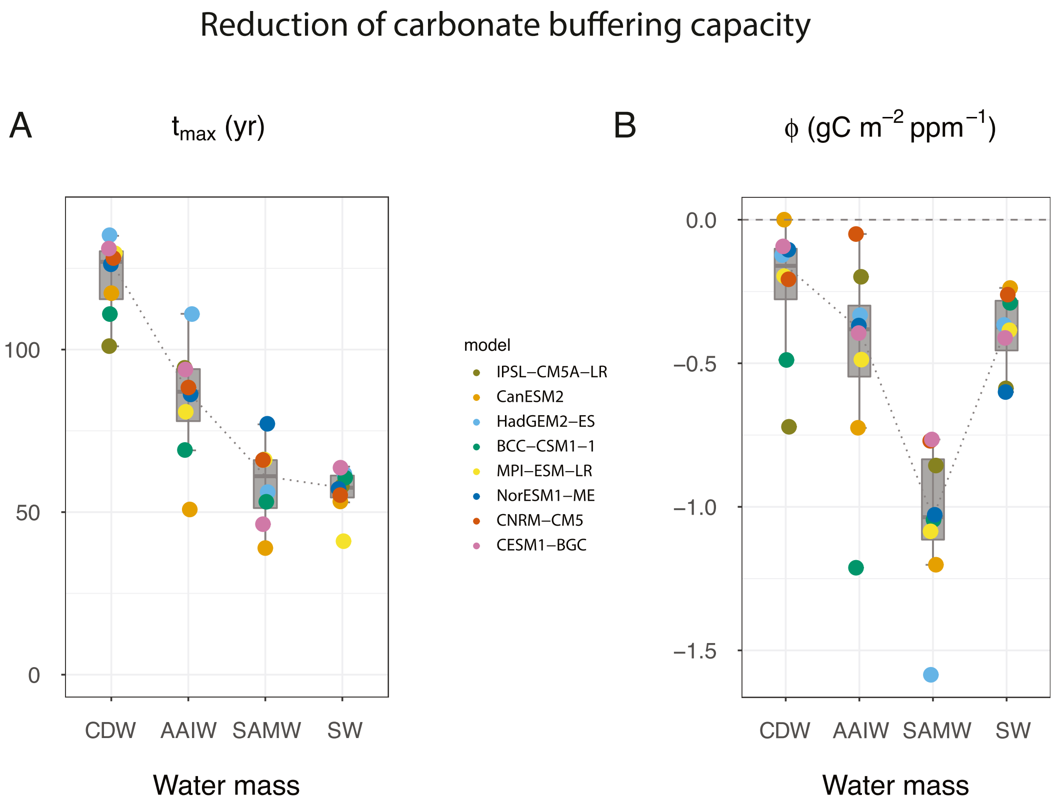

FIG. 8. The impact of the reduction in the carbonate buffering capacity on the projected change in the air–sea CO_2 flux. (a) t_{max} (yr) and the (b) buffering sensitivity parameter ϕ_{wm} ($gC\,m^{-2}\,ppm^{-1}$) for each model and SO water mass. The horizontal gray line, box, and whiskers represent the multimodel median, the IQR, and the 5th–95th percentile limits, respectively.

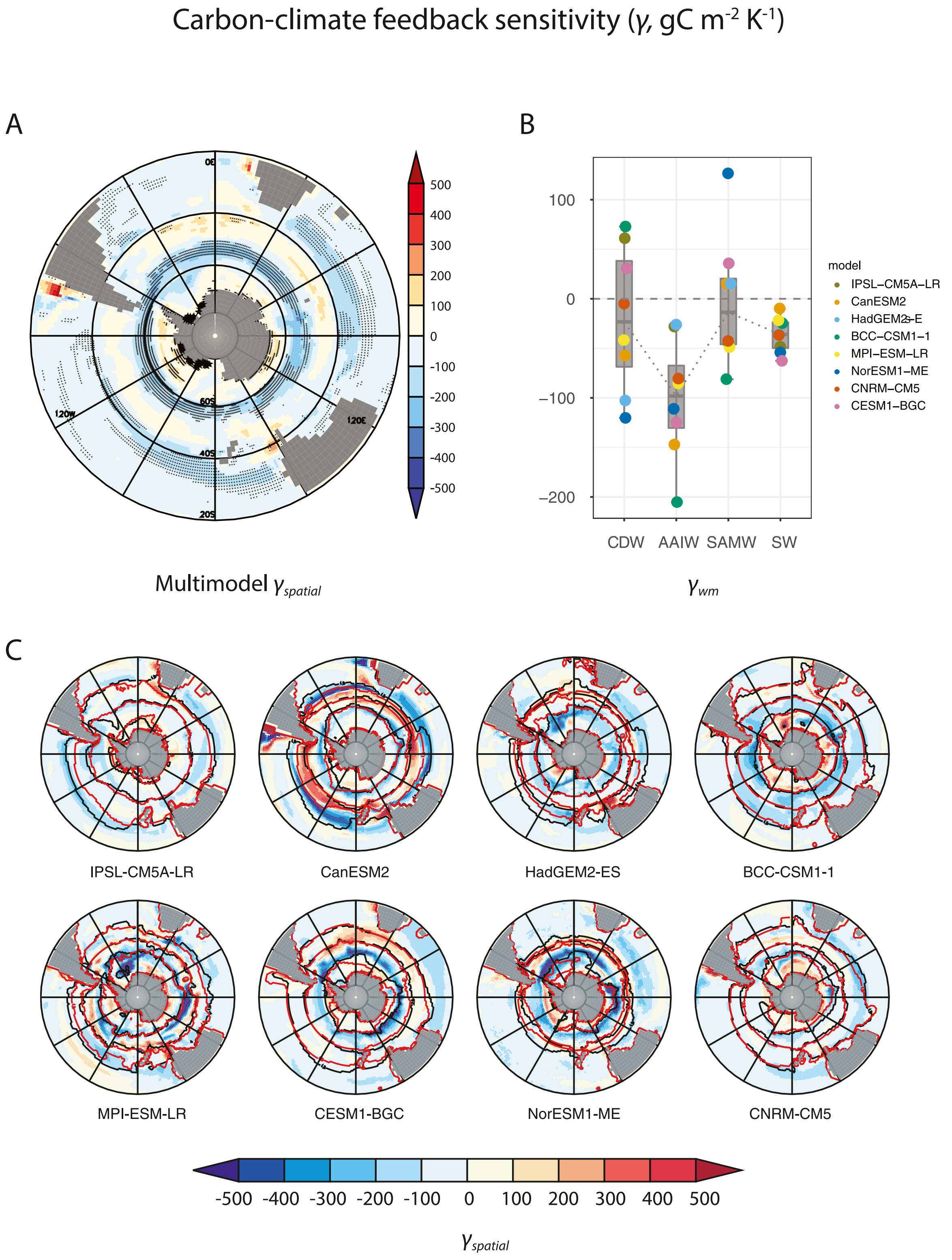

FIG. 9. The SO carbon–climate feedback sensitivity parameter γ ($\mathrm{gC\,m^{-2}\,K^{-1}}$) in the CMIP5 models: (a) Multimodel mean spatially resolved γ, $\gamma_{\mathrm{spatial}}$. The stippled regions represent where the $\gamma_{\mathrm{spatial}}$ of the ESM simulations all have the same sign. (b) Water mass–averaged γ, γ_{wm}. The multimodel median and IQR are represented by the gray box plots. The horizontal gray line, box, and whiskers represent the multimodel median, the IQR, and the 5th–95th percentile limits, respectively. (c) The spatial distribution of γ, $\gamma_{\mathrm{spatial}}$, for each CMIP5 model. The black contours represent the preindustrial boundaries (t_0) of the SO outcrop surface areas and the red contours represent the boundaries at the end of the simulation (t_{140}). The γ_{wm} of each model and SO water mass are tabulated in supplementary material S3.

in all models, while the sign in SAMWs and CDWs is less consistent (Fig. 9b). The AAIWs have the strongest and consistently negative γ across all models, indicating a large reduction in CO_2 uptake across the water mass outcrop area. The most negative γ values in the Southern Hemisphere ocean (Figs. 9c) tend to coincide with where deep DIC rich waters are either obducted or transported northward (Fig. 4b).

1) LOCAL CLIMATE IMPACT FEEDBACK (ΔCCLIM_LOC)

Local climate impacts reduce the multimodel cumulative (140 yr) change in CO_2 uptake (ΔCclim_loc) by −27 PgC (IQR: 5 PgC, Fig. 10a, Table 3). The largest reductions occur over the AAIWs (−11 PgC, IQR: 8 PgC) and are associated with the strong negative γ here (Fig. 9b). We would expect the reduction in CO_2 uptake here to be associated with the most consistent changes in the ocean circulation among the ESMs (Fig. 10b): primarily the strengthening of the upper overturning cell and weakening of the lower circulation cell (Sallée et al. 2013b; Meijers 2014) that is associated with the intensified northward surface circulation driven by increased westerly wind intensity (Bracegirdle et al. 2013) and the shallowing of the mixed layers.

It is likely that the large reductions in carbon uptake along the southern sections of the AAIW outcrop regions are linked to the increased outgassing of natural carbon, which, in the circumpolar AAIW average, masks the increased uptake of anthropogenic CO_2 in the localized zones of AAIW subduction farther north (Sallée et al. 2013b). Model studies and observational records over the historical period in the AAIW outcrop support such a mechanism. Here, pCO_2o was observed to be increasing faster than pCO_2a (Metzl 2009; Takahashi et al. 2012), leading to a reduction in CO_2 uptake, but longer records are required to verify whether this is a trend or linked to large interannual variability in the region. It has been well documented in modeling studies that the strengthening and intensification of zonal winds increases the upwelling of deep DIC-rich waters, and in turn increases pCO_2o and reduces the CO_2 uptake efficiency in the region (Le Quéré et al. 2007; Lovenduski et al. 2007).

Although the CDW outcrop is a net upwelling region, the γ here is more variable in sign and weaker in intensity relative to AAIW (Fig. 9b), we expect this is partly due to the positive and negative regional contributions to γ that are driven by different processes: (i) the increased obduction of CDW induced by increased wind stress in the northern section, which results in the increased natural outgassing of CO_2 and negative γ here; and (ii) the reduction of sea ice in the southern section, which also increases light penetration and, combined with the increased nutrient supply, increases biological production over the region (Laufkötter et al. 2015; Hauck et al. 2015), resulting in positive γ here (Roy et al. 2011).

The sign and magnitude of γ of SAMW and SW have been attributed to both increased temperatures (solubility feedback) and stratification (circulation feedback) (Yoshikawa et al. 2008; Roy et al. 2011). We expect that the intermodel variability in the sign of γ of SAMW depends on the relative contribution of processes with opposing impacts on Δf. A reduction in CO_2 uptake in this region occurs due to large-scale warming (Roy et al. 2011), while an increase in CO_2 uptake is likely in the region in response to the increase in primary production (Leung et al. 2015), which would be further modulated by interactions between changes in the seasonality of biological production and the buffering capacity (Hauck and Volker 2015). It would be valuable to investigate the interactions between atmospheric CO_2 uptake, biological production and β here in future studies.

2) OUTCROP SURFACE AREA FEEDBACK (ΔCCLIM_OS)

The impact of changing outcrop areas on the multimodel cumulative (140 yr) change in Southern Ocean CO_2 uptake (ΔCclim_os) is small (−3 PgC, IQR 3 PgC, Fig. 10a, Table 3 and supplemental material S2) due to the offsetting contributions from different water masses (Fig. 10a), which are largely proportional to changes in the outcrop surface areas of the water masses (Fig. 5d). The ΔCclim_os is largest over the CDWs (−9 PgC, IQR: 10 PgC). Here, the reduction in carbon uptake is associated with contraction of their outcrop areas in response to the expansion of the lighter water masses (Fig. 10b). Since the lighter water masses have lower CO_2 uptake capacity and shorter ventilation times, this could lead to reduced efficiency in longer-term carbon storage.

We expect the changes in the outcrop areas to be associated with changes to the large-scale features of the Southern Ocean circulation (Meijers et al. 2012). The multimodel median outcrop area of the SW increases due the southward expansion of the STGs (Fig. 10b). STGs were found to increase in strength and shift poleward in response to the southward displacement of the westerlies (Russell et al. 2007; Meijers et al. 2012; Meijers 2014; Bracegirdle et al. 2020). The multimodel median outcrop area of the SAMW decreases (Fig. 5d) due to the poleward displacement of the northern SAMW boundary in response to the expansion of the STGs. The multimodel median of AAIW outcrop area increases (Fig. 5d) and is likely associated with the increase in the width of the ACC where AAIW subducts. An increase in ACC area was found to be correlated with an increase in ACC strength (Wang et al. 2011; Meijers et al. 2012). The multimodel median outcrop areas of CDW decreases and is likely related to a decrease in the areal extent of the Weddell and Ross SPGs, decreasing the total area where CDW can obduct. The magnitude and sign of the changes in SPG area were found to be gyre specific and extremely variable between the models and climate scenarios (Meijers et al. 2012), a decrease in SPG area was correlated with an increase in the ACC transport and area, and sometimes with a poleward shift in ACC transport—and vice versa for an increase in the SPG extent. Consistent with this relationship, the only model with an increasing CDW outcrop area (HadGEM2-ES, Fig. 5d) exhibited strong equatorward expansion of both the Weddell and Ross SPGs (Meijers et al. 2012).

Although the intermodel variability of the changes in outcrop area is similar for all water masses (Fig. 5d), the intermodel variability in ΔCclim_os (Fig. 10a) is largest for the CDW (Fig. 10a): (IQRs: 10 PgC) because of its stronger uptake capacity per unit area (Fig. 6b). Given (i) the significant contribution of surface outcrop areas to the magnitude and

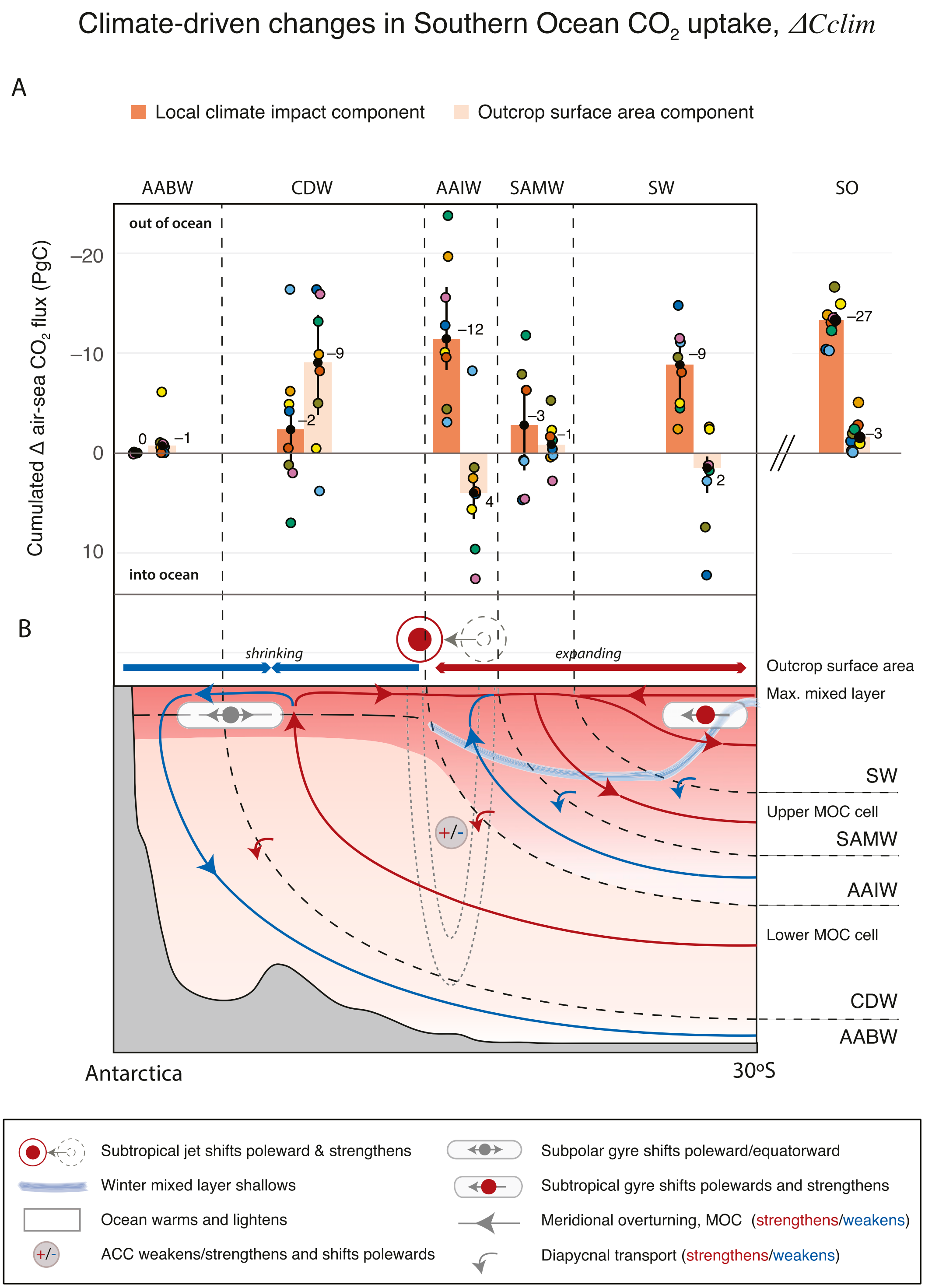

FIG. 10. The cumulated change in the air–sea CO$_2$ flux (ΔCclim, PgC) and the potential ocean circulation mechanisms associated with carbon–climate feedback (γ). (a) The two components of ΔCclim over the SO and each of its water masses: (i) ΔCclim_loc (dark red)—the component driven by local climate impacts and (ii) ΔCclim_os (light red)—the component driven by changes in the outcrop areas. Note these are the same quantities and color schemes used in the summary Fig. 10. The multimodel median and IQR are represented filled black circle and whiskers, respectively. Colored circles represent the individual CMIP5 models (see Fig. 4 for the CMIP5 model key). Positive values signify more ocean uptake of atmospheric CO$_2$. (b) Schematic of the future CMIP5 multimodel ocean circulation changes (Meijers et al. 2012; Bracegirdle et al. 2013; Sallée et al. 2013a,b; Meijers 2014) that are expected to contribute to the carbon–climate feedback.

TABLE 3. The climate change–driven (Δ*C*clim_os and Δ*C*clim_loc; PgC) contributions to the cumulative (140 yr) change in atmospheric CO_2 uptake over the SO south of 20°S (Δ*C*so; PgC) and each of the major SO water masses for each ESM used in this study.

	Δ*C*clim_os						Δ*C*clim_loc						Δ*C*clim
Model	SW	SAMW	AAIW	CDW	AABW	SO	SW	SAMW	AAIW	CDW	AABW	SO	SO
IPSL-CM5A-LR	7	−5	1	−5	−1	−2	−10	−8	−4	1	0	−21	−23
CanESM2	−3	0	3	−10	−1	−10	−2	1	−20	−6	0	−28	−38
HadGEM2-ES	3	0	−8	4	−1	−2	−11	1	−3	−16	0	−30	−32
BCC_CSM1.1	2	−1	10	−13	−1	−4	−4	−12	−24	7	0	−33	−37
MPI-ESM-LR	−2	−2	6	0	−6	−6	−5	−6	−10	−5	0	−26	−32
NorESM1-ME	12	0	4	−16	0	0	−15	5	−13	−4	0	−27	−27
CNRM-CM5	1	−2	4	−8	0	−5	−8	−6	−10	0	0	−24	−29
CESM1(BGC)	1	3	13	−16	−1	0	−12	5	−16	2	0	−20	−21
Median	1	−1	4	−9	−1	−3	−9	−3	−11	−2	0	−27	−30
IQR	4	2	4	10	1	3	6	8	8	7	0	5	7

intermodel variability in carbon uptake by CDWs, and (ii) that the CDW outcrop area is a key region in the global ocean that will continue to have a strong atmospheric CO_2 uptake capacity into the future, it will be important to identify the key factors controlling the dynamics, and thus areal extent of the SPGs—including the westerlies wind belt, the easterlies along the Antarctic coast, and open ocean convection.

5. Synthesis and perspectives

We have developed an automated approach (SO-APT) to objectively track boundaries and outcrop areas of key water masses in the Southern Ocean as their positions and properties evolve under climate change. The approach provides a valuable interpretive context for the complex set of interactions between the oceanic dynamics and the carbon cycle in the Southern Ocean. It can be applied efficiently in multimodel studies and model–data comparisons to define water mass boundaries when a subjective ‘‘eyeballing’’ approach is infeasible. We encourage independent research groups to apply the same water mass boundaries to increase collaboration and to benefit from cross-study comparisons.

We have applied SO-APT to investigate the impact of carbon cycle feedbacks on carbon uptake by the Southern Ocean and its constituent water masses in multiple Earth system models. Carbon-cycle feedbacks increase the multimodel cumulative change in CO_2 uptake by the Southern Ocean relative to the preindustrial (256 PgC, IQR: 75 PgC, Table 4), which amounts to approximately one-quarter of the anthropogenic CO_2 emissions taken up by the global ocean and land reservoirs over the 140-yr simulations (cf. to Arora et al. 2020).

The increase in CO_2 uptake by the Southern Ocean is primarily driven by the dpCO_2 feedback (326 PgC, Table 2, Fig. 11a), with AAIWs making the most substantial contribution (106 PgC). The dpCO_2-driven increase in CO_2 uptake is offset by a ~25% decrease in response to the remaining three secondary carbon cycle feedbacks: carbonate buffering capacity, local climate impacts, and outcrop surface areas (−80 PgC, Fig. 11a)—with maximum reductions in SAMWs.

The feedbacks dominating the decrease in CO_2 uptake is water mass dependent (Figs. 11b,c). The carbonate buffering capacity feedback dominates the reduction in carbon uptake in SWs and SAMWs, presumably due to their low DIC/ALK ratios, high surface to volume ratios, and the recirculation and reemergence of anthropogenic CO_2 in the region. The local climate impact feedback dominates the reduction in carbon uptake in AAIWs and is likely associated with the increased outgassing of carbon associated with the acceleration of the

TABLE 4. The atmospheric CO_2-driven (Δ*C*conc; PgC) and climate change–driven (Δ*C*clim; PgC) contributions to the cumulative (140 yr) change in atmospheric CO_2 uptake over the SO south of 20°S (ΔC_{SO}; PgC) and each of its water masses for each ESM used in this study.

	Δ*C*conc						Δ*C*clim						
Model	SW	SAMW	AAIW	DW	AABW	SO	SW	SAMW	AAIW	DW	AABW	SO	Δ*C*so
IPSL-CM5A-LR	56	113	149	23	3	344	−2	−13	−3	−4	−1	−23	321
CanESM2	30	59	80	88	1	259	−5	1	−17	−16	−1	−38	221
HadGEM2-ES	58	29	59	130	1	276	−8	1	−11	−13	−1	−32	245
BCC_CSM1.1	29	73	125	109	2	337	−3	−13	−14	−6	−1	−37	300
MPI-ESM-LR	49	64	112	111	9	345	−7	−9	−4	−5	−6	−32	313
NorESM1-ME	95	36	110	53	0	294	−3	4	−9	−21	0	−27	267
CNRM-CM5	37	60	40	47	0	183	−7	−8	−6	−9	0	−29	154
CESM1(BGC)	48	44	90	67	1	251	−10	7	−3	−14	−1	−21	230
Median	48	59	100	78	1	285	−6	−3	−7	−11	−1	−30	256
IQR	21	25	40	58	2	82	5	12	8	8	1	7	75

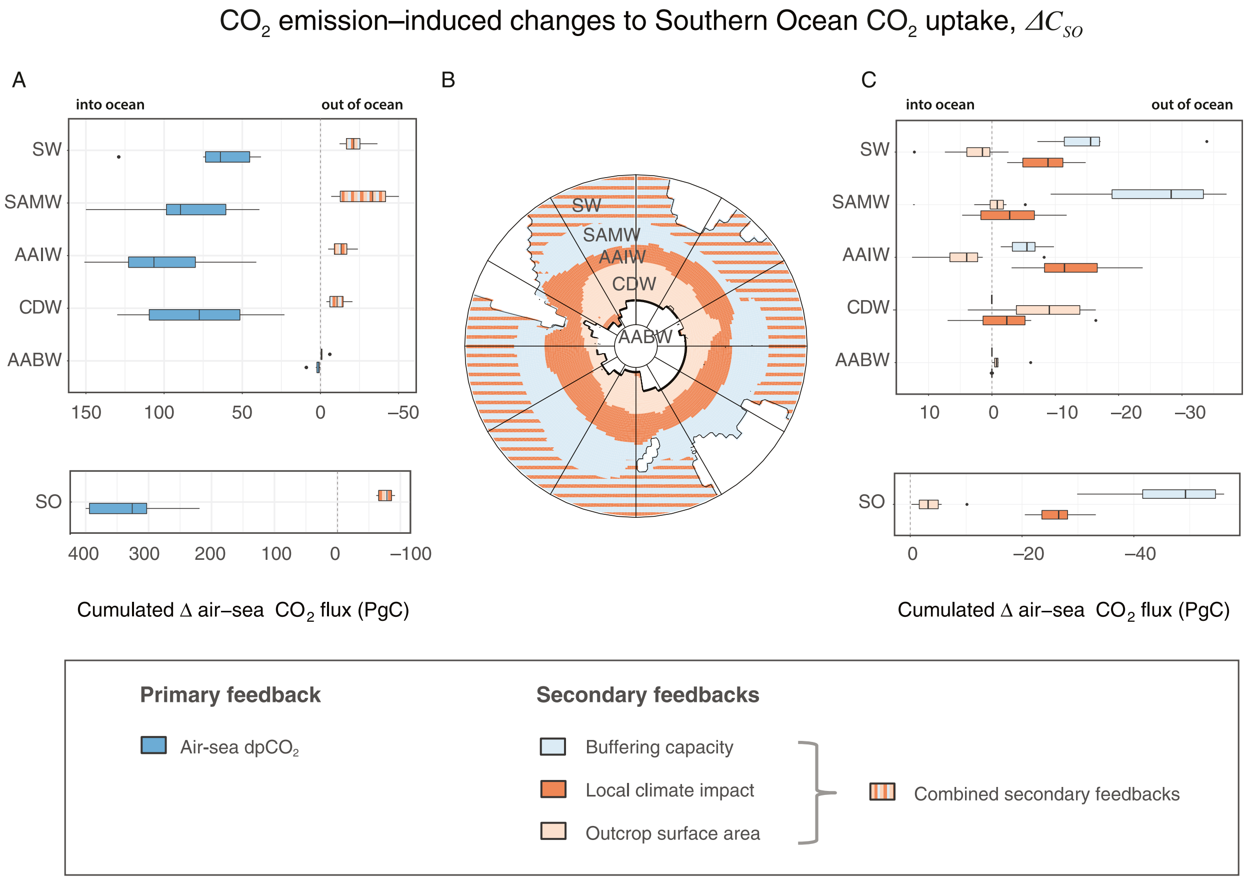

FIG. 11. Summary figure of the multimodel impact of carbon cycle feedbacks on the CO_2-emission-induced cumulated change in the air–sea CO_2 fluxes over the SO (ΔC_{SO}, PgC) and each of its major water masses (ΔC_{wm}, PgC). The box represents the multimodel median and the IQR and the whiskers the 5th–95th percentile limits. The two ΔC components associated with the carbon–concentration feedbacks are colored in blue: ΔCconc_dpCO_2 (dark blue)—the component driven by air–sea CO_2 partial pressure difference, dpCO_2. The ΔC components associated with the carbon–climate feedbacks are colored in red: (i) ΔCclim_loc (dark red) is the component driven by local climate impacts, and (ii) ΔCclim_os (light red) is the component driven by changes in the outcrop areas. Note these are the same quantities and color schemes used in Figs. 6 and 9. (a) The ΔC associated with the primary and dominant feedback (ΔCconc_dpCO_2) and the combined secondary feedbacks (ΔCconc_buff +ΔCclim_loc + ΔCclim_os; striped boxes). (b) Map of dominant secondary feedbacks (ΔCconc_buff, ΔCclim_loc, ΔCclim_os) for each SO water mass. (c) The ΔC associated with the individual secondary feedbacks.

upper cell of the meridional overturning circulation—one of the most robust climate-driven changes in the CMIP5 models. The outcrop surface area feedback dominates the reduction in carbon uptake in CDWs, and intermodel variability in its magnitude is likely associated with changes to the subpolar gyre extent from the south and the ACC area from the north. An important caveat is that the estimate of the carbonate buffering capacity feedback would be larger if diagnosed more precisely and would potentially dominate in all water masses.

The carbonate buffering capacity component of the carbon–concentration feedback is the strongest negative Southern Ocean carbon cycle feedback (−49 PgC, IQR 13 PgC, Table 2, Fig. 11c), and would be significantly higher if estimated precisely. Although the impact of diminishing carbonate buffering capacity on carbon uptake is well understood, it is not sufficiently evaluated in current generations of ESMs. A more precise diagnostic of the buffer capacity feedback (Katavouta and Williams 2021) and a comprehensive study of the mechanisms contributing to its spatiotemporal variability are required to characterize this major carbon cycle feedback. Similar mechanisms contribute to ocean acidification (Resplandy et al. 2013) and will be critical to projections of the impact of carbon cycle feedbacks on future ocean acidification (Matear and Lenton 2018). Climate-driven carbon–climate feedbacks make a relatively minor contribution to the decrease in Southern Ocean carbon uptake (−30 PgC, Table 4).

The intermodel variability in the projected CO_2 uptake is dominated by the dpCO_2 feedback (IQR: 90 PgC, Table 2) and largely stems from AAIWs and CDWs (Fig. 11a, IQRs: 43 PgC and 58 PgC, Table 2) and should be a focus of efforts to constrain projection uncertainty. This intermodel variability is most likely associated with the variable representation of WM formation rates in the upwelling regions of the Southern Ocean and the areal extent of the upwelling region.

We argue that the dpCO_2 feedback is most likely underestimated in the full set of CMIP5 models because (i) the strength in the $dpCO_2$ feedback depends on the strength of Southern Ocean upwelling, and (ii) the CMIP5 models have been shown to underestimate the strength of upwelling in the divergence zone of the Southern Ocean (Sallée et al. 2013b, and summarized in Fig. 10b)—and is consistent with the underestimate of historical Southern Ocean CO_2 uptake by the ESMs (Frölicher et al. 2015). This would have two important implications: (i) projected CO_2 uptake by the Southern Ocean is underestimated in the models, leading to an underestimate of the cumulative CO_2 emissions allowable for a given global warming target, and (ii) air–sea CO_2 fluxes themselves should be useful constraints on projected CO_2 uptake.

The Southern Ocean moderates Earth's climate not only by the uptake of anthropogenic CO_2 emissions, but also by the uptake of excess heat (Durack et al. 2014), which varies by as much as 40% in the ESMs (Frölicher et al. 2015). Understanding and quantifying the mechanisms driving intermodel variability in carbon and heat uptake/storage is key to finding effective constraints on the uncertainty in future projections of Earth's climate system. We propose that consistent water mass frameworks should be applied to subsequent generations of ESMs to analyze changes in the Southern Ocean circulation and to track the associated heat and carbon uptake from the ocean surface into the ocean interior—thereby deepening our mechanistic understanding of the evolution of heat and carbon in the Southern Ocean over the coming century.

Acknowledgments. This project has received funding from the European Commission's FP7 project under Grant Agreement 264879 (CARBOCHANGE) and the European Union's Horizon 2020 Research and Innovation Programme under Grant Agreements 821001 (SO–CHIC project) and 820989 (COMFORT). We are also grateful to the reviewers for their valuable contributions.

Data availability statement. The CMIP5 data are publicly available at https://esgf-node.llnl.gov/projects/cmip5/.

REFERENCES

Arora, V. K., and Coauthors, 2011: Carbon emission limits required to satisfy future representative concentration pathways of greenhouse gases. *Geophys. Res. Lett.*, **38**, L05805, https://doi.org/10.1029/2010GL046270.

——, and Coauthors, 2013: Carbon–concentration and carbon–climate feedbacks in CMIP5 Earth system models. *J. Climate*, **26**, 5289–5314, https://doi.org/10.1175/JCLI-D-12-00494.1.

——, and Coauthors, 2020: Carbon–concentration and carbon–climate feedbacks in CMIP6 models and their comparison to CMIP5 models. *Biogeosciences*, **17**, 4173–4222, https://doi.org/10.5194/bg-17-4173-2020.

Bindoff, N. L., and T. J. McDougall, 2000: Decadal changes along an Indian Ocean section at 32°S and their interpretation. *J. Phys. Oceanogr.*, **30**, 1207–1222, https://doi.org/10.1175/1520-0485(2000)030<1207:DCAAIO>2.0.CO;2.

Boer, G. J., and V. Arora, 2010: Geographic aspects of temperature and concentration feedbacks in the carbon budget. *J. Climate*, **23**, 775–784, https://doi.org/10.1175/2009JCLI3161.1.

Bracegirdle, T. J., E. Shuckburgh, J.-B. Sallée, Z. Wang, A. J. S. Meijers, N. Bruneau, T. Phillips, and L. J. Wilcox, 2013: Assessment of surface winds over the Atlantic, Indian, and Pacific Ocean sectors of the Southern Ocean in CMIP5 models: Historical bias, forcing response, and state dependence. *J. Geophys. Res. Atmos.*, **118**, 547–562, https://doi.org/10.1002/jgrd.50153.

——, C. R. Holmes, J. S. Hosking, G. J. Marshall, M. Osman, M. Patterson, and T. Rackow, 2020: Improvements in circumpolar Southern Hemisphere extratropical atmospheric circulation in CMIP6 compared to CMIP5. *Earth Space Sci.*, **7**, e2019EA001065, https://doi.org/10.1029/2019EA001065.

Cao, M., and F. I. Woodward, 1998: Dynamic responses of terrestrial ecosystem carbon cycling to global climate change. *Nature*, **393**, 249–252, https://doi.org/10.1038/30460.

Ciais, P., and Coauthors, 2013: Carbon and other biogeochemical cycles. *Climate Change 2013. The Physical Science Basis*, T. F. Stocker et al., Eds., Cambridge University Press, 465–570.

Collins, W. J., and Coauthors, 2011: Development and evaluation of an Earth-system model—HadGEM2. *Geosci. Model Dev.*, **4**, 1051–1075, https://doi.org/10.5194/gmd-4-1051-2011.

Cox, P. M., R. A. Betts, C. D. Jones, S. A. Spall, and I. J. Totterdell, 2000: Acceleration of global warming due to carbon-cycle feedbacks in a coupled climate model. *Nature*, **408**, 184–187, https://doi.org/10.1038/35041539.

Downes, S. M., N. L. Bindoff, and S. R. Rintoul, 2009: Impacts of climate change on the subduction of mode and intermediate water masses in the Southern Ocean. *J. Climate*, **22**, 3289–3302, https://doi.org/10.1175/2008JCLI2653.1.

Dufresne, J. L., and Coauthors, 2013: Climate change projections using the IPSL-CM5 Earth System Model: From CMIP3 to CMIP5. *Climate Dyn.*, **40**, 2123–2165, https://doi.org/10.1007/s00382-012-1636-1.

Durack, P. J., P. J. Gleckler, F. W. Landerer, and K. E. Taylor, 2014: Quantifying underestimates of long-term upper-ocean warming. *Nat. Climate Change*, **4**, 999–1005, https://doi.org/10.1038/nclimate2389.

Egleston, E. S., C. L. Sabine, and F. M. M. Morel, 2010: Revelle revisited: Buffer factors that quantify the response of ocean chemistry to changes in DIC and alkalinity. *Global Biogeochem. Cycles*, **24**, GB1002, https://doi.org/10.1029/2008GB003407.

Friedlingstein, P., J. L. Dufresne, P. M. Cox, and P. Rayner, 2003: How positive is the feedback between climate change and the carbon cycle? *Tellus*, **55B**, 692–700, https://doi.org/10.3402/tellusb.v55i2.16765.

——, and Coauthors, 2006: Climate-carbon cycle feedback analysis: Results from the (CMIP)-M-4 model intercomparison. *J. Climate*, **19**, 3337–3353, https://doi.org/10.1175/JCLI3800.1.

Frölicher, T. L., J. L. Sarmiento, D. J. Paynter, J. P. Dunne, J. P. Krasting, and M. Winton, 2015: Dominance of the Southern Ocean in anthropogenic carbon and heat uptake in CMIP5 models. *J. Climate*, **28**, 862–886, https://doi.org/10.1175/JCLI-D-14-00117.1.

Gregory, J. M., C. D. Jones, P. Cadule, and P. Friedlingstein, 2009: Quantifying carbon cycle feedbacks. *J. Climate*, **22**, 5232–5250, https://doi.org/10.1175/2009JCLI2949.1.

Gruber, N., P. Landschützer, and N. S. Lovenduski, 2019: The variable Southern Ocean carbon sink. *Annu. Rev. Mar. Sci.*, **11**, 159–186, https://doi.org/10.1146/annurev-marine-121916-063407.

Hauck, J., and C. Volker, 2015: Rising atmospheric CO_2 leads to large impact of biology on Southern Ocean CO_2 uptake via changes of the Revelle factor. *Geophys. Res. Lett.*, **42**, 1459–1464, https://doi.org/10.1002/2015GL063070.

——, and Coauthors, 2015: On the Southern Ocean CO_2 uptake and the role of the biological carbon pump in the 21st century.

Global Biogeochem. Cycles, **29**, 1451–1470, https://doi.org/10.1002/2015GB005140.

Hewitt, A. J., B. B. B. Booth, C. D. Jones, E. S. Robertson, A. J. Wiltshire, P. G. Sansom, D. B. Stephenson, and S. Yip, 2016: Sources of uncertainty in future projections of the carbon cycle. *J. Climate*, **29**, 7203–7213, https://doi.org/10.1175/JCLI-D-16-0161.1.

Hobbs, W. R., C. Roach, T. Roy, J.-B. Sallée, and N. Bindoff, 2021: Anthropogenic temperature and salinity changes in the Southern Ocean. *J. Climate*, **34**, 215–228, https://doi.org/10.1175/JCLI-D-20-0454.1.

Ilyina, T., K. D. Six, J. Segschneider, E. Maier-Reimer, H. Li, and I. Núñez-Riboni, 2013: Global ocean biogeochemistry model HAMOCC: Model architecture and performance as component of the MPI-Earth system model in different CMIP5 experimental realizations. *J. Adv. Model. Earth Syst.*, **5**, 287–315, https://doi.org/10.1029/2012MS000178.

Iudicone, D., K. B. Rodgers, I. Stendardo, O. Aumont, G. Madec, L. Bopp, O. Mangoni, and M. R. d'Alcala, 2011: Water masses as a unifying framework for understanding the Southern Ocean carbon cycle. *Biogeosciences*, **8**, 1031–1052, https://doi.org/10.5194/bg-8-1031-2011.

——, ——, Y. Plancherel, O. Aumont, T. Ito, R. M. Key, G. Madec, and M. Ishii, 2016: The formation of the ocean's anthropogenic carbon reservoir. *Sci. Rep.*, **6**, 35473, https://doi.org/10.1038/srep35473.

Jiang, L.-Q., B. R. Carter, R. A. Feely, S. K. Lauvset, and A. Olsen, 2019: Surface ocean pH and buffer capacity: Past, present and future. *Sci. Rep.*, **9**, 18624, https://doi.org/10.1038/s41598-019-55039-4.

Jones, C., and Coauthors, 2013: Twenty-first-century compatible CO_2 emissions and airborne fraction simulated by CMIP5 Earth system models under four representative concentration pathways. *J. Climate*, **26**, 4398–4413, https://doi.org/10.1175/JCLI-D-12-00554.1.

Joos, F., G.-K. Plattner, T. F. Stocker, O. Marchal, and A. Schmittner, 1999: Global warming and marine carbon cycle feedbacks on future atmospheric CO_2. *Science*, **284**, 464–467, https://doi.org/10.1126/science.284.5413.464.

Katavouta, A., and R. G. Williams, 2021: Ocean carbon cycle feedbacks in CMIP6 models: Contributions from different basins. *Biogeosciences*, **18**, 3189–3218, https://doi.org/10.5194/bg-18-3189-2021.

Khatiwala, S., F. Primeau, and T. Hall, 2009: Reconstruction of the history of anthropogenic CO_2 concentrations in the ocean. *Nature*, **462**, 346–349, https://doi.org/10.1038/nature08526.

Landschützer, P., and Coauthors, 2015: The reinvigoration of the Southern Ocean carbon sink. *Science*, **349**, 1221–1224, https://doi.org/10.1126/science.aab2620.

Laufkötter, C., and Coauthors, 2015: Drivers and uncertainties of future global marine primary production in marine ecosystem models. *Biogeosciences*, **12**, 6955–6984, https://doi.org/10.5194/bg-12-6955-2015.

Le Quéré, C., and Coauthors, 2007: Saturation of the Southern Ocean CO_2 sink due to recent climate change. *Science*, **316**, 1735–1738, https://doi.org/10.1126/science.1136188.

Leung, S., A. Cabre, and I. Marinov, 2015: A latitudinally banded phytoplankton response to 21st century climate change in the Southern Ocean across the CMIP5 model suite. *Biogeosciences*, **12**, 5715–5734, https://doi.org/10.5194/bg-12-5715-2015.

Lindsay, K., and Coauthors, 2014: Preindustrial-control and twentieth-century carbon cycle experiments with the Earth system model CESM1(BGC). *J. Climate*, **27**, 8981–9005, https://doi.org/10.1175/JCLI-D-12-00565.1.

Lovenduski, N. S., N. Gruber, S. C. Doney, and I. D. Lima, 2007: Enhanced CO 2outgassing in the Southern Ocean from a positive phase of the southern annular mode. *Global Biogeochem. Cycles*, **21**, GB2026, https://doi.org/10.1029/2006GB002900.

Maier-Reimer, E., U. Mikolajewicz, and A. Winguth, 1996: Future ocean uptake of CO_2: Interaction between ocean circulation and biology. *Climate Dyn.*, **12**, 711–722, https://doi.org/10.1007/s003820050138.

Marshall, J., and K. Speer, 2012: Closure of the meridional overturning circulation through Southern Ocean upwelling. *Nat. Geosci.*, **5**, 171–180, https://doi.org/10.1038/ngeo1391.

Matear, R. J., and A. C. Hirst, 1999: Climate change feedback on the future oceanic CO_2 uptake. *Tellus*, **51B**, 722–733, https://doi.org/10.3402/tellusb.v51i3.16472.

——, and A. Lenton, 2018: Carbon–climate feedbacks accelerate ocean acidification. *Biogeosciences*, **15**, 1721–1732, https://doi.org/10.5194/bg-15-1721-2018.

McNeil, B. I., N. Metzl, R. M. Key, R. J. Matear, and A. Corbière, 2007: An empirical estimate of the Southern Ocean air–sea CO_2 flux. *Global Biogeochem. Cycles*, **21**, GB3011, https://doi.org/10.1029/2007GB002991.

Meijers, A. J. S., 2014: The Southern Ocean in the coupled model intercomparison project phase 5. *Philos. Trans. Roy. Soc.*, **A372**, 20130296, https://doi.org/10.1098/rsta.2013.0296.

——, E. Shuckburgh, N. Bruneau, J. B. Sallée, T. J. Bracegirdle, and Z. Wang, 2012: Representation of the Antarctic Circumpolar Current in the CMIP5 climate models and future changes under warming scenarios. *J. Geophys. Res.*, **117**, C12008, https://doi.org/10.1029/2012JC008412.

Metzl, N., 2009: Decadal increase of oceanic carbon dioxide in southern Indian Ocean surface waters (1991–2007). *Deep-Sea Res. II*, **56**, 607–619, https://doi.org/10.1016/j.dsr2.2008.12.007.

——, B. Tilbrook, and A. Poisson, 1999: The annual fCO_2 cycle and the air–sea CO_2 flux in the sub-Antarctic Ocean. *Tellus*, **51B**, 849–861, https://doi.org/10.3402/tellusb.v51i4.16495.

Mikaloff-Fletcher, S. E., and Coauthors, 2007: Inverse estimates of the oceanic sources and sinks of natural CO_2 and the implied oceanic carbon transport. *Global Biogeochem. Cycles*, **21**, GB1010, https://doi.org/10.1029/2006GB002751.

Nakano, H., M. Ishii, K. B. Rodgers, H. Tsujino, and G. Yamanaka, 2015: Anthropogenic CO_2 uptake, transport, storage, and dynamical controls in the ocean imposed by the meridional overturning circulation: A modeling study. *Global Biogeochem. Cycles*, **29**, 1706–1724, https://doi.org/10.1002/2015GB005128.

Plattner, G. K., F. Joos, T. F. Stocker, and O. Marchal, 2001: Feedback mechanisms and sensitivities of ocean carbon uptake under global warming. *Tellus*, **53B**, 564–592, https://doi.org/10.3402/tellusb.v53i5.16637.

Resplandy, L., L. Bopp, J. C. Orr, and J. P. Dunne, 2013: Role of mode and intermediate waters in future ocean acidification: Analysis of CMIP5 models. *Geophys. Res. Lett.*, **40**, 3091–3095, https://doi.org/10.1002/grl.50414.

Revelle, R., and H. E. Suess, 1957: Carbon dioxide exchange between atmosphere and ocean and the question of an increase of atmospheric CO_2 during the past decades. *Tellus*, **9**, 18–27, https://doi.org/10.3402/tellusa.v9i1.9075.

Ridgway, K. R., J. R. Dunn, and J. L. Wilkin, 2002: Ocean interpolation by four-dimensional weighted least squares—Application to the waters around Australasia. *J. Atmos. Oceanic Technol.*, **19**, 1357–1375, https://doi.org/10.1175/1520-0426(2002)019<1357:OIBFDW>2.0.CO;2.

Roy, T., and Coauthors, 2011: Regional impacts of climate change and atmospheric CO_2 on future ocean carbon uptake:

A multimodel linear feedback analysis. *J. Climate*, **24**, 2300–2318, https://doi.org/10.1175/2010JCLI3787.1.

Russell, J. L., R. J. Stouffer, and K. W. Dixon, 2007: Intercomparison of the Southern Ocean circulations in IPCC coupled model control simulations. *J. Climate*, **20**, 4287–4287, https://doi.org/10.1175/JCLI3869.1; Corrigendum, **19**, 4560, https://doi.org/10.1175/JCLI4326.1.

——, and Coauthors, 2018: Metrics for the evaluation of the Southern Ocean in coupled climate models and Earth system models. *J. Geophys. Res. Oceans*, **123**, 3120–3143, https://doi.org/10.1002/2017JC013461.

Sabine, C. L., and Coauthors, 2002: Distribution of anthropogenic CO_2 in the Pacific Ocean. *Global Biogeochem. Cycles*, **16**, 1083, https://doi.org/10.1029/2001GB001639.

Sallée, J.-B., K. Speer, S. Rintoul, and S. Wijffels, 2010: Southern Ocean thermocline ventilation. *J. Phys. Oceanogr.*, **40**, 509–529, https://doi.org/10.1175/2009JPO4291.1.

——, E. Shuckburgh, N. Bruneau, A. J. S. Meijers, T. J. Bracegirdle, and Z. Wang, 2013a: Assessment of Southern Ocean mixed-layer depths in CMIP5 models: Historical bias and forcing response. *J. Geophys. Res. Oceans*, **118**, 1845–1862, https://doi.org/10.1002/jgrc.20157.

——, ——, ——, ——, ——, ——, and T. Roy, 2013b: Assessment of Southern Ocean water mass circulation and characteristics in CMIP5 models: Historical bias and forcing response. *J. Geophys. Res. Oceans*, **118**, 1830–1844, https://doi.org/10.1002/jgrc.20135.

Salt, L. A., S. M. A. C. van Heuven, M. E. Claus, E. M. Jones, and H. J. W. de Baar, 2015: Rapid acidification of mode and intermediate waters in the southwestern Atlantic Ocean. *Biogeosciences*, **12**, 1387–1401, https://doi.org/10.5194/bg-12-1387-2015.

Sarmiento, J. L., 2013: *Ocean Biogeochemical Dynamics*. Princeton University Press, 528 pp.

——, and C. Le Quéré, 1996: Oceanic carbon dioxide uptake in a model of century-scale global warming. *Science*, **274**, 1346–1350, https://doi.org/10.1126/science.274.5291.1346.

——, ——, and S. W. Pacala, 1995: Limiting future atmospheric carbon dioxide. *Global Biogeochem. Cycles*, **9**, 121–137, https://doi.org/10.1029/94GB01779.

——, T. M. C. Hughes, R. J. Stouffer, and S. Manabe, 1998: Simulated response of the ocean carbon cycle to anthropogenic climate warming. *Nature*, **393**, 245–249, https://doi.org/10.1038/30455.

Schwinger, J., and Coauthors, 2014: Nonlinearity of ocean carbon cycle feedbacks in CMIP5 Earth system models. *J. Climate*, **27**, 3869–3888, https://doi.org/10.1175/JCLI-D-13-00452.1.

Séférian, R., D. Iudicone, L. Bopp, T. Roy, and G. Madec, 2012: Water mass analysis of effect of climate change on air–sea CO_2 fluxes: The Southern Ocean. *J. Climate*, **25**, 3894–3908, https://doi.org/10.1175/JCLI-D-11-00291.1.

Siegenthaler, U., and H. Oeschger, 1978: Predicting future atmospheric carbon dioxide levels. *Science*, **199**, 388–395, https://doi.org/10.1126/science.199.4327.388.

Sigman, D. M., M. P. Hain, and G. H. Haug, 2010: The polar ocean and glacial cycles in atmospheric CO_2 concentration. *Nature*, **466**, 47–55, https://doi.org/10.1038/nature09149.

Takahashi, T., C. Sweeney, B. Hales, D. Chipman, T. Newberger, J. Goddard, R. Iannuzzi, and S. Sutherland, 2012: The changing carbon cycle in the Southern Ocean. *Oceanography*, **25**, 26–37, https://doi.org/10.5670/oceanog.2012.71.

Taylor, K. E., R. J. Stouffer, and G. A. Meehl, 2012: An overview of CMIP5 and the experiment design. *Bull. Amer. Meteor. Soc.*, **93**, 485–498, https://doi.org/10.1175/BAMS-D-11-00094.1.

Tjiputra, J. F., C. Roelandt, M. Bentsen, D. M. Lawrence, T. Lorentzen, J. Schwinger, Ø. Seland, and C. Heinze, 2013: Evaluation of the carbon cycle components in the Norwegian Earth System Model (NorESM). *Geosci. Model Dev.*, **6**, 301–325, https://doi.org/10.5194/gmd-6-301-2013.

Voldoire, A., and Coauthors, 2013: The CNRM-CM5.1 global climate model: Description and basic evaluation. *Climate Dyn.*, **40**, 2091–2121, https://doi.org/10.1007/s00382-011-1259-y.

Wallace, D. W. R., 2001: Storage and transport of excess CO2 in the oceans: The JGOFS/WOCE global CO_2 survey. *Ocean Circulation and Climate: Observing and Modelling the Global Ocean*, G. Siedler, J. Church, and J. Gould, Eds., International Geophysics Series, Vol. 77, 489–521, Academic Press, https://doi.org/10.1016/S0074-6142(01)80136-4.

Wang, Z., T. Kuhlbrodt, and M. P. Meredith, 2011: On the response of the Antarctic Circumpolar Current transport to climate change in coupled climate models. *J. Geophys. Res.*, **116**, C08011, https://doi.org/10.1029/2010JC006757.

Wu, T., and Coauthors, 2013: Global carbon budgets simulated by the Beijing Climate Center Climate System Model for the last century. *J. Geophys. Res. Atmos.*, **118**, 4326–4347, https://doi.org/10.1002/jgrd.50320.

Yoshikawa, C., M. Kawamiya, T. Kato, Y. Yamanaka, and T. Matsuno, 2008: Geographical distribution of the feedback between future climate change and the carbon cycle. *J. Geophys. Res.*, **113**, G03002, https://doi.org/10.1029/2007JG000570.

Zeebe, R. E., and D. Wolf-Gladrow, 2001: *CO_2 in Seawater: Equilibrium, Kinetics, Isotopes*. Elsevier Oceanography Series, Vol. 65, Elsevier Science, 360 pp.